ABSTRACT

Title of dissertation: PARICLE MOTION
IN GRANULAR MATERIALS:
THREE DIMENSIONAL IMAGING
OF SLOW FLOWS
AND COMPACTION

Steven Charles Slotterback,
Doctor of Philosophy, 2012

Dissertation directed by: Professor Wolfgang Losert
Department of Physics

Granular materials have been a subject of study for centuries. Their bulk properties are well known and are quite reproducible. However, it is not well understood how motions at the grain level relate to bulk behaviors. In this thesis, we describe the use of a 3D imaging technique to determine the motions of individual grains in known geometries.

We use a method known as the Refractive Index-Matched Scanning (RIMS) method to locate and track centers of individual grains in dense granular piles. This method enables us to capture grain scale rearrangements where other techniques, such as displacement field imaging, may fail. We may also track motions of grains with respect to their nearest neighbors in order to measure local flows.

We first apply the RIMS method to the study of a gentle compaction process, known as thermal cycling. We track the centers of grains between temperature cycles, capturing cycle-to-cycle displacements. The tracks are used to generate

dynamic Voronoi volumes about the centers of grains at each cycle. We are able to observe fluctuations in the shapes of the Voronoi volumes which correlate strongly with subsequent motion of grains. We find that the grains move preferentially toward the centroid of the vertices of their respective Voronoi cells.

We then study grain motions in quasistatic flows in a split-bottom geometry. We observe nearest neighbor separation events during both steady and cyclic shearing processes. We find a critical strain beyond which there is a qualitative change in the breakage of contacts between neighbors. Cyclic shear flows with amplitudes below this critical strain settle into a nearly reversible flow pattern, while those with amplitudes above the critical strain remain in a persistent diffusive, irreversible state.

Overall, the RIMS method is a powerful tool for probing the structure of slow granular flows. We are now able to examine particle level rearrangements which were previously explored in simulations. Furthermore, with a modification of the image processing technique, it is possible to apply the RIMS method to the study of other sorts of granular flows, such as those with bidisperse grains, or even those with detectable orientations.

PARICLE MOTION IN GRANULAR MATERIALS: THREE DIMENSIONAL IMAGING OF SLOW FLOWS AND COMPACTION

by

Steven Charles Slotterback

Dissertation submitted to the Faculty of the Graduate School of the
University of Maryland, College Park in partial fulfillment
of the requirements for the degree of
Doctor of Philosophy
2012

Advisory Committee:
Professor Wolfgang Losert, Chair/Advisor
Professor Derek Richardson, Dean's Representative
Professor Michelle Girvan
Professor Victor Yakovenko
Dr. Jack Douglas

Dedication

to Mary Ann Mullen (1934-2007) and Gijs Katgert (1981-2011)

Acknowledgments

"If I have seen a little further it is by standing on the shoulders of Giants."-Sir Isaac Newton

I would like to thank Wolfgang Losert for working with me throughout my graduate career. His guidance and insight have proven invaluable in many situations.

I thank my collaborators, Jack Douglas, Martin Van Hecke, and Michelle Girvan, for their help and insight that has made a great impact on my work. I would also like to thank Wim Van Saarloos for helpful discussions.

I owe a great deal of success to the past and current members of Dr. Losert's Granular Dynamics Lab, Masahiro Toiya, Mike Newey, Krisztian Ronaszegi, Joshua Dijksman, Joost Weijs, Mark Herrera, Matt Harrington, and Kerstin Nordstrom for their help and guidance over the years. I thank Mitch Mailman especially for acting almost as a second advisor towards the end of my graduate studies. I thank Don Martin for providing his expert guidance in the construction of various pieces of experimental apparatus. I would also like to thank the various undergraduate students, Len Goff, Emmanuel Cephas Jr., Khalid Ismail, Nick Prior, Chris Berardi, Derek Updegraff, and Michael Lin for their assistance in my endeavors. Finally, I thank the members of the Biophysics Lab sharing ideas and equipment with me.

I am thankful for the excellent staff in both the Physics Department and IREAP, as they have been more than helpful in making the day-to-day aspects of graduate research much easier.

Last but not least, I must thank my family and friends for their love and

support through the years.

Table of Contents

List of Figures

List of Abbreviations

CMSD	Cumulative Mean Square Displacement
CT	Computerized Tomography
DEM	Discrete Element Modeling
IREAP	Institute for Research in Electronics and Applied Physics
MSD	Mean Square Displacement
NMR	Nuclear Magnetic Resonance
PDF	Probability Distribution Function
PMMA	Poly(methyl methacrylate)
PMP	Polymethylpentene
POVRay	Persistence of Vision Raytracer
PTV	Particle Tracking Velocimetry
RIMS	Refractive Index-Matched Scanning
RPM	Revolutions Per Minute

Chapter 1

Introduction

This thesis describes an experimental study of motion of individual grains of dense granular matter in a state of flow. Granular materials exhibit rich, multi-phase behaviors which set them apart in the study of soft condensed matter. Despite the fact that the dynamics of the grains fall within the regime of deterministic contact force kinematics, it is still an open question as to how grain-level contact forces together lead to the well-known bulk behaviors. We introduce a Refractive Index-Matched Scanning (RIMS) approach to probe the motions of entire ensembles of grains in dynamic granular ensembles to further our understanding of the relationship between microscopic dynamics and bulk behaviors.

1.1 Motivation

Granular materials are perhaps the most common form of aggregate matter. We see these bulk solids every day, whether they be sand on the beach, the flour in our kitchens, or the rock salt that we store up in our garages for the winter. They are also common in industrial applications, including but not limited to: food processing (grains, salts, sugars), fluidized bed reactors (coal combustion), or even construction (concrete, asphalt, etc.). There are also several well-known extraterrestrial granular materials, such as the regolith of the near earth asteroid 433 Eros [4] or even our moon [5].

All granular materials have some basic physical properties in common. They all consist of a large ensemble of solid particles, ranging in size from microns to meters across. The grains interact almost exclusively through contact forces, specifically normal forces and frictional forces. Such forces are repulsive and dissipative in nature, meaning that grains only move when a force is applied, and grain motion dies down shortly after. It is possible for grains to have mutually cohesive forces when a liquid bridge forms between neighboring grains, leading to many different bulk properties [6]. In this work, we only consider “dry” granular materials. We do however study grains without attractive forces due to liquid bridges and surface tension that are completely immersed in a liquid, as we will show in Section 4.2.

1.2 Properties of Granular Materials

In some ways, granular materials act as a different state of matter. They can exhibit solid-like properties, such as a sand dune that maintains its overall shape even when walked upon. However, under sufficient stresses, they can be made to flow as a liquid, like sand through an hourglass. This dual nature has been studied by scientists and engineers for centuries, from the work of Coulomb on retaining walls [7], continuing to the work of Bagnold on sand dunes [8], Beverloo on hopper flows [9], and many others.

Granular flows, particularly dense granular flows, are quite complex. For slow flows, the grains are constantly colliding with and rolling or sliding alongside their neighbors, rapidly dissipating kinetic energy added to the system. On the other hand, grains in rapid flows can have enough kinetic energy to break away from their neighbors to follow more ballistic trajectories. Sometimes, as in the case of chute flows (inclined planes) and avalanches, a flow can have both slow and rapid flows occuring within a few grain lengths of one another, with a rapid flow on the surface and the slow flow beneath the surface [10]. Other examples of complex granular flows include, but are not limited to, banded shear flows [11], segregation of different sized grains (radial and axially) in rotating drums [12], and jet formations upon impact by a rapidly approaching intruder [13].

Much of the earlier theoretical work in granular materials applied a continuum approach to the behavior of granular flows. For instance, in Mohr-Coulomb theory, a granular material undergoes flow under stress in a "plane" of failure (which is indeed several grain diameters thick) [14]. This failure occurs when the shear stress along the plane of failure is equal to or in excess of the internal static frictional forces, following the Mohr-Coulomb criterion:

$$\tau \geq \mu\sigma + c \tag{1.1}$$

where σ is the principal stress perpendicular to the failure plane, μ is an empirical friction coefficient, τ is the shear stress along the plane of failure, and c is an empirical cohesion factor (usually zero for dry granular materials) [15]. This type of failure leads to the typical cone shape seen in sandpiles (see Figure 1.1).

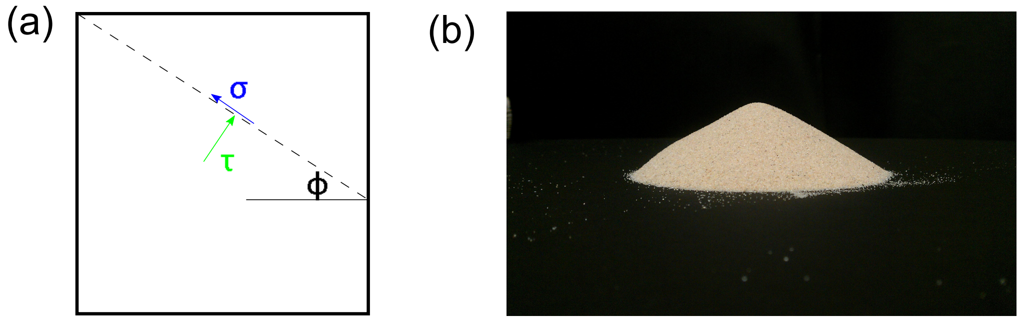

Figure 1.1: (a) Illustration of Coulomb model of granular failure of a cohesionless vertical column. Note that the angle of repose, ϕ, is related to the normal (τ) and shear (σ) stresses by the relation $\tan\phi = \sigma/\tau$. (b) A cone-shaped sandpile formed by a fallen vertical column.

1.3 A Microscopic View of Granular Materials

The continuum approach, although useful for explaining bulk behavior, does not fully account for the underlying dynamics of granular flows, such as segregation of grains according to size. In recent years, the study of granular materials has expanded to include measurements of motions at the grain level underlying bulk behaviors. For example, Pierre-Gilles de Gennes compared critical migrations of magnetic flux densities in superconductors to avalanches in sand hills [16], noting that both had no underlying models at the time. Since then, there have been many studies of granular flows, both theoretical [17] and experimental [18, 19] to probe the nature of such critical behaviors. (We now know that some theories, such as self-organized criticality, do not hold for all cases [20].)

Despite the many-body nature of granular materials, they do not typically lend themselves to a conventional statistical mechanics analysis. For example, a single grain of sand of size 100 μm and density 2 g/mL requires roughly 10^{-10}J of energy to travel one grain diameter upward against gravity, while typical thermal fluctuations at room temperature (300 K) are merely $\approx 10^{-21}$J; small enough to be considered negligible. Thus, a granular material may be considered to be an athermal mechanical system, in that the ensemble can only change state (e.g. packing fraction) when subjected to mechanical forcing, rather than exploring a "phase phase" as an equilibrium statistical mechanical system would do.

1.3.1 Static indeterminance

Furthermore, granular materials can not be modeled with the methods of classical mechanics. At the grain level, a granular material has a complex fabric of contact forces. Individual grains are held in place by their nearest neighbors. For a typical densely packed three-dimensional system, grains are in contact with six of their nearest neighbors on average [21] (assuming sphere shaped grains). We know from Newtonian mechanics that, for a body in static equilibrium, the sum of the forces and torques balance each other out [22]. However, we do not have enough constraints to determine the possible configurations for a given number of particles analytically. A simple example of an indeterminate static system, shown in Figure 1.2, has many possible solutions due to the existence of static friction.

In Figure 1.2, a single disk of mass m and radius R rests on two frictional surfaces with frictional coefficient μ under the influence of gravity. The frictional forces may vary, depending on how the disk is set onto the surfaces. If we assume

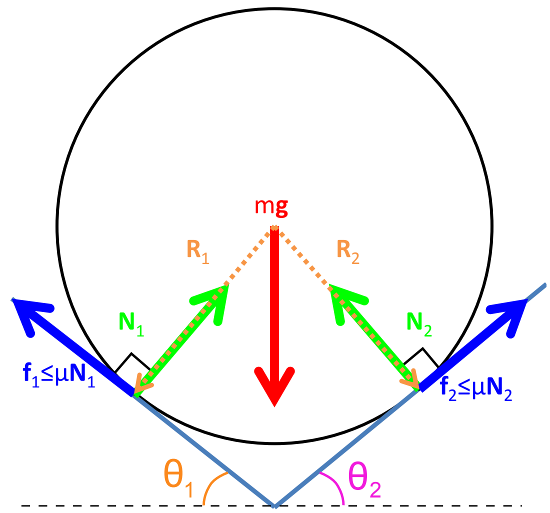

Figure 1.2: Free Body Diagram of Simple Indeterminate 2D Mechanical System

that the system is in equilibrium, we have the following relations between forces:

$$\vec{0} = m\vec{g} + \vec{N_1} + \vec{N_2} + \vec{f_1} + \vec{f_2} \tag{1.2}$$

$$\vec{0} = \vec{R_1} \times \vec{f_1} + \vec{R_2} \times \vec{f_2} \tag{1.3}$$

$$|\vec{f_1}| \leq \mu|\vec{N_1}| \tag{1.4}$$

$$|\vec{f_2}| \leq \mu|\vec{N_2}| \tag{1.5}$$

where m is the mass of the disk, g is acceleration due to gravity, R is the disk radius, f is a frictional force of the disk on a surface, μ is the coefficient of static friction between the disk and a surface, and N is the normal force between the disk and a surface. The given constraints are insufficient for resolving the exact forces acting on the disk, save for the frictionless case (i.e. $\mu = 0$).

In a three dimensional system, a granular ensemble can be similarly unsolvable. For each grain in equilibrium, there are six degrees of freedom (3 translational and

3 rotational). These equations can be solved if grains have on average four contact forces (assuming the forces are not strictly central forces) [23]. However, for a typical granular ensemble, grains can have on average 6 contacts with neighboring grains [24], making typical granular ensembles underdetermined.

1.4 Theoretical and Experimental Studies of Granular Flows at the Grain Level

It is because of this indeterminacy that the nature of grain-level dynamics of granular materials is an open problem. Theorists and experimentalists alike employ various empirical methods to observe various grain scale behaviors of test systems.

1.4.1 Theoretical Models

Theorists have adapted numerical methods originally used in the study of condensed matter. They use Discrete Element Modeling (DEM) methods wherein trajectories of grains are evaluated in a step-wise fashion, integrated for short time intervals [25]. Interactions between grains are typically modeled by a soft sphere potential $V_{ij}(r)$ with a finite range, . This soft sphere potential is defined as follows:

$$V_{ij}(r) \equiv \begin{cases} \frac{\epsilon}{\alpha}\left(1 - \frac{r}{\sigma}\right)^{\alpha} & r \leq \sigma \\ 0 & r > \sigma \end{cases} \tag{1.6}$$

where r is the radial displacement of the two grains, α is an exponent that is varied to express different potentials (i.e. 2 for Hookean and $\frac{5}{2}$ for Hertzian), σ is the sum of the radii of two interacting particles i and j, and ϵ is an adjustable physical parameter corresponding to the strength of the interaction. Forces are calculated from these potentials using the relation

$$\vec{f}_{ij} = -\nabla V_{ij}(r)\Big|_{r=r_{ij}} \tag{1.7}$$

Finally, displacements are calculated by integrating the equations of motion:

$$m\ddot{\vec{x}}_i = \sum_{j \neq i} \vec{f}_{ij} \tag{1.8}$$

over short time intervals. This process is continued for as many time intervals as desired, with the forces reevaluated at the start of each new time interval.

For dense granular shear flows, they sometimes apply a special periodic boundary condition known as Lees-Edwards boundaries [26]. It is also possible to incorporate other physical features, such as friction [27], or even non-spherical shapes, such as ellipses or tetrahedra.

1.4.2 Experimental Methods

There have been many advances in experimental methods for imaging the grain-level motions in granular materials. For instance, CCD cameras have made it possible to directly image grains in a dense flow in many situations [28, 29, 30, 31]. The trajectories of grains in these experiments are found using methods such as those developed by Crocker et al [32]. These methods are precise, yet limited to 2D systems and surface layers.

It is also possible to use photoelastic disks to measure force transmission in 2D granular ensembles. Such materials experience birefringence under stress. Thus, when a dense ensemble of photoelastic grians is placed between a pair of crossed polarizers, grains that experience greater stresses transmit more light. This technique allows us to directly visualize how grains transmit stress in both static and flowing systems. [33, 34, 35]

There are also methods for probing the internal motions in dense granular flows. Internal imaging devices using NMR [36, 37] or X-ray tomography [38, 39, 2, 40] have been used to highlight the internal flows of dense granular ensembles. Such methods have provided insights into the internal structure of dense granular piles in both static and flowing systems. In this thesis, we will explore a different imaging method, known as the Refractive Index-Matched Scanning (RIMS) method to further examine granular flows.

1.5 Open Problems in Granular Materials

The theoretical and experimental techniques mentioned above allow us to ask various questions regarding the grain-level behavior. Below are three examples of open questions regarding granular flows, and how the RIMS method can be used to address them.

1.5.1 The Collective Motion Question

How do grains move with respect to their neighbors in a dense flow? We know that grains in dense ensembles are constrained by their neighbors. However, the specifics of how forces on the bulk induce grain-level motion is not fully understood.

One study done by Ellembroek et al. explored a dense ensemble at the onset of flow [41]. In this work, the grains, modeled by soft disks, were initially densely packed. When the ensemble is perturbed locally, the grains several grain diameters away move in response. Furthermore, the mobile grains predominately roll or slide past the neighbors with which they are in contact.

We use our RIMS approach to study collective dynamics of all grains in the context of several different flows. In Chapter 3, we consider the rearrangements of grains during a compaction process. In Chapters 4 and 5, we study how the grains rearrange in quasistatic steady and cyclic shear processes, respectively.

1.5.2 The Intermediate Scale Question

Once we know how the grains move locally, how do we relate these local flows to the bulk behavior of the entire ensemble? Are there intermediate, meso-scale features which we can use to relate the grain level motion to bulk flow? Are these mesoscale features generic, or specific to different types of flow?

In Chapters 4 and 5, we will explore some mesoscopic properties of a granular shear flow using a nearest neighbor network reconstruction of our ensemble. This network reconstruction allows us to probe dynamics of shear flows at multiple scales, from single pairs of neighboring grains to the entire system. We can observe how pairs of neighbors connect and separate in a flow, as well as how those connection/separation events propagate during a shear flow process.

1.5.3 The Reversibility Question

Another question we ask is how reversible grain rearrangements are in a dense granular flow? For instance, suppose a granular pile is subjected to a shear stress with a strain of γ. If the same system is then subjected to a strain $-\gamma$, do the grains revert to their original positions?

We specifically explore the question of reversibility of granular flows in Chapter 5. We measure the degree to which the individual grains, as well as their initial network of nearest neighbors, are reversible over a range of cyclic strain amplitudes.

1.6 Scope of Thesis

This thesis shall be concerned with the study of slow granular flows at the grain level. In Chapter 2, we introduce the Refractive Index-Matched Scanning method, which we use to analyze granular flow. This novel method allows us to create three-dimensional tomographic images of dense granular piles so that we can precisely locate the centroids of all individual grains. We use Particle Tracking Velocimetry (PTV) to determine trajectories for all grains in a slow moving system. Once the motion of individual grains is known, we can also determine how grains move relative to their neighbors.

In Chapter 3, we will use the RIMS method to measure the grain-level motions within a gentle compaction process. Compaction by thermal cycling proves to be a good testing ground for the RIMS technique since the grains do not shift significantly during the compaction process. We calculate the trajectories of all grains between temperature cycles. We show that the local arrangement of nearest neighbors is strongly correlated with the motion of individual grains between cycles.

Chapter 4 will address the application of RIMS to a granular ensemble subject to quasistatic shear. We use a split-bottom geometry in order to induce a shear zone within the bulk of the ensemble, so that wall effects are negligible. We find that, at sufficiently low strain rates, the ensemble behaves as a dry granular system, even when immersed in a viscous fluid. Furthermore, as the strain on the system is increased, we note that the fraction of initial nearest neighbors lost increases suddenly, suggesting a topological change in the system under shear.

We explore this sudden topological change further in Chapter 5. We reverse the direction of strain on our ensemble in this case to study how reversible the motions of grains are in a shear process. We discover that over several cycles of forward and reverse strain, there is also a sudden change in the dynamics of our system when the amplitude is increased. Beyond a certain strain amplitude, the dynamics of the grains and their neighbors goes from being increasingly reversible from cycle-to-cycle, to consistently irreversible from cycle-to-cycle. This suggests a critical strain amplitude which "breaks" the configuration of a granular pile.

Finally in Chapter 6, we will consider other ways in which RIMS may be applied to the study of dense granular flows. The image processing methods may be modified to measure rotations in asymmetric grains or even segregation of bidisperse grains. Perhaps the greatest challenge for the RIMS method would be the adaptation of the process for the study of rapid granular flows, such as those induced by impacts of projectiles.

Chapter 2

PTV Methods For Dense Granular Packings

In this chapter, we will discuss the experimental methods to track the grains in a dense granular pile in 3 dimensions. We introduce the **R**efractive **I**ndex-**M**atched **S**canning (RIMS) technique to illuminate cross-sections of the pile for tomographic imaging. Using this technique, we can create a faithful 3D reconstruction of a dense granular ensemble with high spatial resolution. I made refinements to the index matching, image acquisition, and image analysis to improve quality of the data, working with several visiting students, particularly Krisztian Ronaszegi, Joshua Dijksman, and Joost Weijs. These methods allow us to then locate the centers of all grains using digital image processing. This process is crucial for recreating the trajectories of all of the grains using **P**article **T**racking **V**elocimetry (PTV) methods. Once we have the trajectories of all grains, we can directly measure collective dynamics in granular ensembles undergoing compaction (Chapter 3), as well as steady (Chapter 4) and cyclic (Chapter 5) shear flows.

2.1 Overview: RIMS Imaging

We are able to find the positions of individual grains in a dense granular materials using the RIMS method. This method was first used by Toiya et al. [42] to monitor local deformations. This method involves the matching of refractive indices of grains, usually glass or plastic balls, with a fluid medium. A ray of light passing from one transparent medium to another is deflected according to Snell's Law:

$$n_1 \sin\theta_1 = n_2 \sin\theta_2 \tag{2.1}$$

where n is the refractive index of a given medium and θ is measured with respect to the surface normal at the interface of the two media. The refractive index n of a medium is defined as the ratio of the speed of light in a vacuum to the speed of light in said medium. When the grains are immersed in an index-matched fluid, light passes through the fluid-grain mixture undeflected.

A low concentration of fluorescent dye of a known absorbtion wavelength is added to the fluid. When we pass a sheet of laser light with the absorption wavelength through the system, we are able to illuminate a cross-section of the fluid, as shown in Figure 2.1(a). These cross-sections, photgraphed by a CCD camera, appear as bright sheets with dark disks corresponding to cross-sections of individual grains (Figure 2.1(b)). The laser sheet is translated ("scanned") through the system in small increments along the z axis. The camera is also translated along the z axis, but at different increment than the laser sheet to account for the change in the apparent position of the laser sheet due to the different optical path length within the fluid. The increments are chosen so that the z axis displacement is identical to the pixel scale in the images of xy planar cross-sections. This isotropic length scale along the x, y, and z axes is highlighted in the reconstructed cross-section in Figure 2.1(c). This method yields a high fidelity three-dimensional image of the entire en-

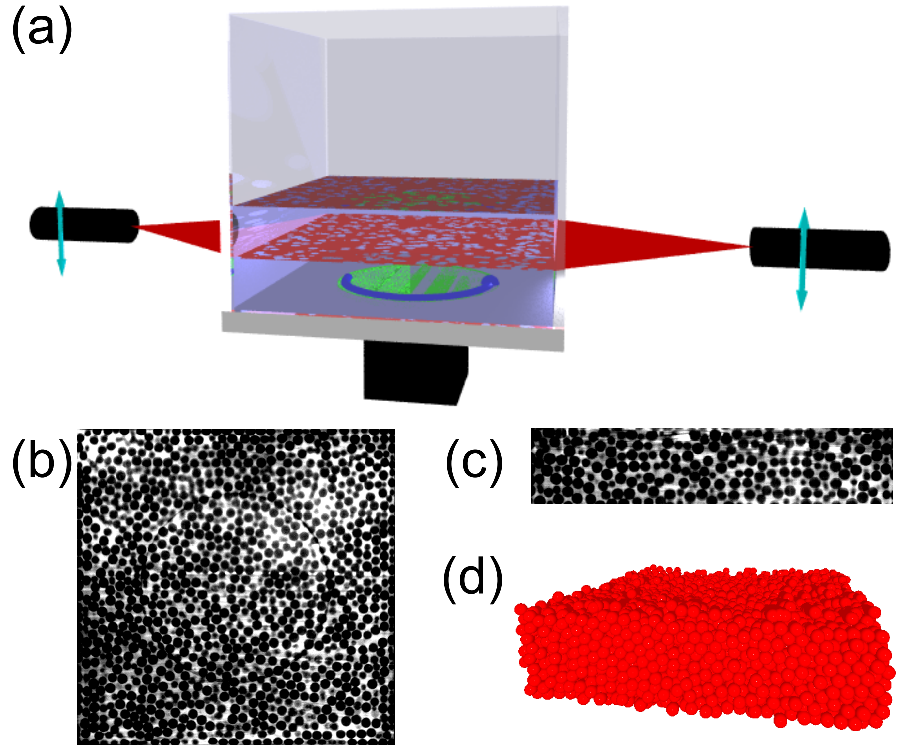

Figure 2.1: (a) Illustration of Typical RIMS apparatus. (b) Sample digital image of horizontal cross-section of system illuminated by laser sheet (contrast enhanced for figure). (c) Sample composite image of vertical cross-section made from a sequential stack of horizontal images (contrast enhanced for figure). (d) Digital rendering of grains based on centers found through digital image processing of stacks of cross-sections.

semble of grains. We address the specifics of the construction and operation of the RIMS apparatus in Appendix A.

One of the first key tasks of this thesis research was to improve RIMS to make the images accurate enough for finding and tracking individual grains. Once a suitable fluid-grain combination is found, we employ several methods that we developed to tune the refractive index of the fluid to match that of the grains. One method is to titrate an additive to the fluid, which changes the effective refractive index of the fluid. Another method is to tune the temperature of the mixture of the system, since refractive indices of most materials are temperature dependent. The fluid is considered sufficiently index matched to the grains when a laser beam can be passed through the fluid-grain mixture with minimal distortion. Note that we must we very precise in our index matching, as the laser sheet passes through many surfaces at various angles with respect to the surface normals.

We used two sets of materials in the course of this research. The thermal cycling experiment (Chapter 3) required the use of soda-lime glass beads, due to the added requirement that the grains have a low thermal expansion coefficient. We used PMMA beads for experiments involving quasistatic flows in the split-bottom geometry (Chapters 4, 5, and 6), as we found that the index-matching between PMMA and Triton X-100 is maintained for prolonged periods of time (2-4 weeks) at room temperature ($\approx 20°$C). A table of the materials used in this work is presented in Table 2.1.

Several other RIMS-appropriate materials have been shown to work in recent years. Dijksman et al [43] have examined the suitability of many different materials and index matching fluids, as well as many imaging considerations.

2.1.1 Advantages of RIMS Imaging Method

The RIMS method has several advantages over other common macroscopic 3D imaging methods, such as X-ray computerized tomography (CT) or Nuclear Magnetic Resonance (NMR) imaging. For instance, all of the equipment used for a

Setup	Thermal Cycling	Split Bottom
Camera	PCO SensiCam 370 KL	PCO SensiCam 370 KL
Laser Wavelength	635 nm	635 nm
Laser Dye Type	Nile Blue 690 Percholorate	Nile Blue 690 Perchlorate
Dye Concentration	1 mg/L	1 mg/L
Bead Material	Soda-Lime Glass	PMMA
Fluid Medium	Cargille Labs: Type DF Immersion Oil	99.9 % Trition X-100, 0.1 % 12 M HCl

Table 2.1: Materials Used For RIMS Imaging

RIMS system is generally in the $20k range (the camera typically being the most expensive item), while CT and NMR scanners cost several times that figure. Also, the RIMS equipment is generally safer to operate, primarily requiring shielding of visible laser light, while the other methods typically require shielding of x-ray radiation and/or high intensity magnetic fields. Thus, a RIMS method is safer and less costly than more commonly known 3D scanning methods.

Also, cost and safety concerns aside, the RIMS method is more conducive to imaging different types of granular flows. For instance, an electric motor may be incorporated into a RIMS-based system, provided it is not within the optical path of the laser sheet or imaging camera. An X-ray CT scanner has stricter spatial constraints, since the sample must be rotated with respect to the X-ray source, or vice versa. An NMR system cannot have metallic components, and would thus require a specialized coupler apparatus for motion control. Thus, a RIMS-based imaging system allows for more straightforward experimental designs for the study of granular flows.

2.1.2 Limitations of RIMS Imaging Method

There are some limitations to the RIMS method. First of all, our axial resolution is limited by the thickness of the laser sheet produced by our current line generator (Coherent Lasiris SNF 501) to ≈ 100 μm for our typical systems. This constrains our choice of grain size to $\approx 1-2$ mm or higher for PTV-based experiments, to allow for at least 10 layers, and thus 10 pixels of resolution for each grain. Objects smaller than ≈ 10 pixels in diameter would be more difficult, if not impossible, to track with appreciable precision.

Another limitation to the RIMS technique is the low tolerance for index mismatches. The refractive index of the fluid can be altered slightly by the unintentional introduction of impurities, such as water, or by fluctuations in temperature as small as 2°C. Even for small mismatches of refractive index between grains and fluid, the laser sheet is deflected by several grain-fluid interfaces over short distances of a few grain diameters. This effect is exacerbated in cases where the grain diameter is smaller, as more interfaces are present in the material. For this reason, great care must be taken to ensure that the refractive indices are well matched in order to obtain useful images for PTV.

A model, constructed using the ray-tracing program POVRay (Persistence of Vision Raytracer [44]), illustrates the sensitivity of the quality of the image to small

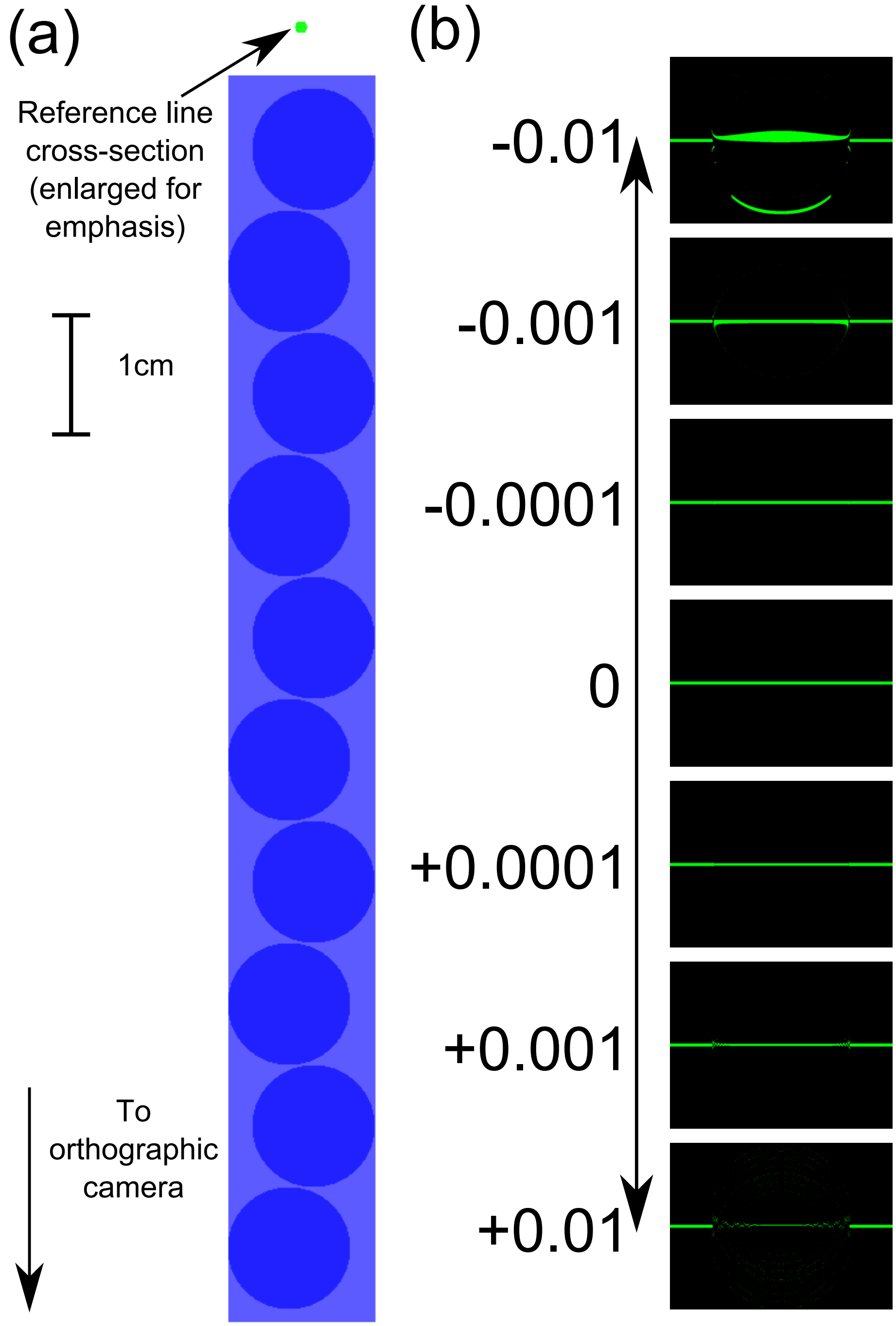

Figure 2.2: Illustration of optical effects on laser sheet caused by mis-matching of refractive index (a) Schematic of model system (b) Far field rendering of optical distortions caused by slight mis-matches of refractive index between beads and interstitial fluid .

discrepances between the refractive indices of beads and fluid (Figure 2.2). In this simulation, ten 10 mm balls with an index of refraction of 1.48899 are placed in contact in a zigzag arrangement. The balls are surrounded by a fluid of refractive index n_f. A rod placed "behind" the ball-fluid system is visually distorted in the frame by small differences between the refractive indices of beads and fluid. The distortions are seen for differences as low as 0.06%. Such a narrow band of tolerance leaves little room for error in preparing the fluid.

2.2 Particle Tracking Velocimetry

Once we have a set of 3D snapshots of the system, we are able to use Particle Tracking Velocimetry (PTV) methods to track the motions of the centers of all the grains in our system. In a typical PTV process, localized bright spots (particles) are located in each of a series of frames. The positions of the particles are then matched with their most likely counterparts in subsequent frames to form trajectories. With this tool, thousands of grains may be tracked across several frames.

We begin with a digital image processing procecdure, wherein we convolve the frames to highlight the centroids of the grains. First, we take the negative of the frames in order to make the grains appear as bright balls. We then employ a 3D spatial low pass filter, with an upper bound set to the presumed grain diameter, to smooth over intensity gradients. We convolve the frame with a specialized edge-finding kernel (see Appendix B for details) to create bright spots centered within the centers of each grain. Finally, we threshold the image to isolate the pixels corresponding to each bright spot, which we find to be mostly symmetric about the local maximum pixel. We take advantage of the symmetric distribution of brightness by taking the weighted averages of intensities for each spot to calculate the centroids of each spot. This process enables us to achieve a precision even finer than the pixel scale. Although we do not attempt to directly calculate a tolerance for our centroid coordinates, we may safely assume that the positions along each axis are accurate to within ± 0.25 pixels (a 0.5 pixel range).

Once we have the centroids of all of our grains in each frames, we track the motions of the centroids between frames. We limit ourselves to applying small perturbations to our system between scans, where almost all of the grains move less than 0.4 grain diameters between frames, to minimize the possibility of an ambiguous set of trajectories (see Figure 2.3). The most common method for matching trajectories between subsequent frames was introduced by Crocker et al. [32]. Briefly, the trajectories between subsequent frames are chosen such that the total square displacement is at a global minimum. We are able to significantly reduce the number of possible trajectories to calculate by the aforementioned strain limitation of our experiments.

2.3 Applications of Trajectories

Once we have faithful trajectories of all the grains, there are many metrics that we can apply to our system to probe our dense granular flows. For instance, we can measure the time evolution of static configurational properties, such as the

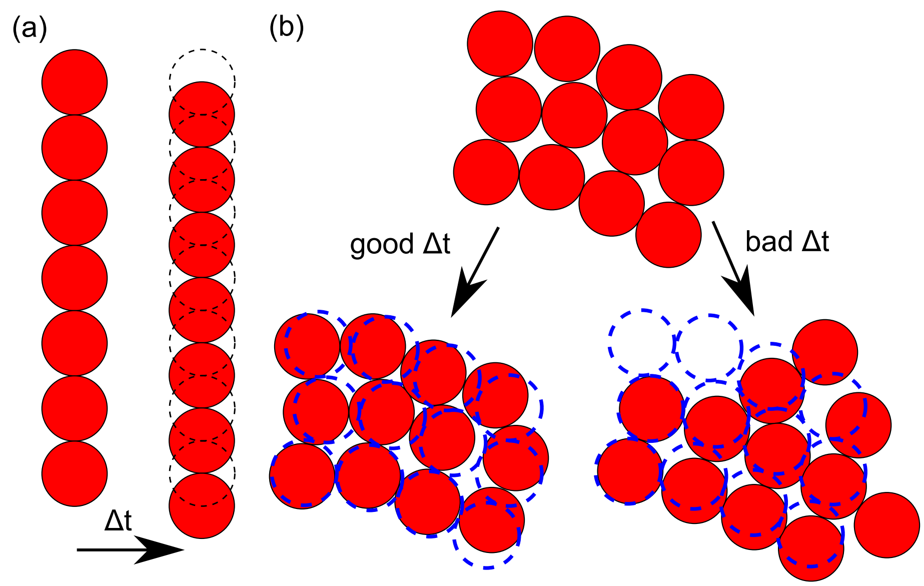

Figure 2.3: (a) Illustration of an ambiguous particle tracking scenario. In this situation, initial positions of interior grains are equidistant from two candidate final positions. (b) An illustration of a disordered ensemble at three example configurations. Initial configuration of grains subjected to some force. If the rate of imaging ($1/\Delta t$) is sufficiently fast, the new positions of grains are all near their previous positions, and will yield unambiguous trajectories. However, if the time interval between frames is too great, the grains may move too far from their initial positions, allowing for many ambiguous possible trajectories.

bond orientational parameter Q_6 [45], which we introduce in Chapter 4. in addition to measuring the time evolution of statistics of the ensemble, we can also measure statistics of the trajectories themselves. We may use the Cumulative Mean Square Displacement (CMSD) to measure how far grains drift from their initial positions with time, as we do in Chapter 5. There are many other metrics that we may apply to the trajectories to understand the grain motions, which we shall introduce in detail in later chapters.

2.4 Summary

In this chapter, we have discussed the use of the RIMS method to construct a faithful representation of a dense granular ensemble. Given the appropriate choice of materials, we are able to image our sample with a high degree of resolution. We are able to go beyond the realm of difference imaging and process the resulting high-resolution images to find centroids of the grains themselves with precision finer than the pixel scale of the initial images. We can then employ a PTV method to construct trajectories from centroids of all grains in consecutive frames of a slow granular flow.

We will use this method to quantify the collective behavior of grains in granular materials in various quasistatic deformation processes. In chapter 3, we will examine the rearrangements in a gentle compaction process, wherein the containing walls slowly expand and contract. In chapter 4, we consider the rearrangements that occur during a steady shear process in a split-bottom geometry. Finally, we will consider the degree of reversibility of a shear process in chapter 5, where we employ a cyclic strain to the aforementioned system.

Chapter 3

Compaction by Thermal Cycling

This chapter is adapted from a publication by Slotterback, Toiya, Goff, Douglas, and Losert [46], wherein I modified Toiya's RIMS method for tracking individual grains, constructed the experimental apparatus, tracked the grains, and defined a volume shape vector to quantify fluctuations in volume local to a given grain.

In this chapter, we use the RIMS technique to track grain motions in a granular material subjected to a gentle compaction process via thermal cycling. Particle displacements in this jammed material correlate strongly with rearrangements of the Voronoi cells defining the local environment about the grains, similar to previous observations by Rahman in cooled liquids [47]. Our observations provide evidence of commonalities between grain dynamics in granular matter close to jamming and supercooled liquids.

3.1 Compaction

Granular materials generally tend to compact under certain forms of stress. This sort of behavior is especially apparent in various food preparation processes. For instance, anyone who has used an espresso machine knows that the coffee grains are tamped down (compressed) into a cartridge prior to being loaded into the machine. Alternatively, if you wanted to fill a sugar container to capacity, you might lightly shake or tap the side of the container until the top level of the sugar went down a bit further. Both methods of compaction are alluded to in the New Testament (Luke 6.38), where a generous quantity of grains is described as being "...pressed down, shaken together and running over ..." [48]. These forms of agitation cause the individual grains to rearrange in order to minimize the empty space between them.

Compaction has been studied for quite some time. There have been both experimental and numerical studies of compaction phenomena in granular materials for cases of tapping [49], shaking [50], and even shearing [29]. However, in most experimental methods, it is only possible to measure bulk properties of the pile, such as the filling height, since most methods of compaction impart a great deal of kinetic energy to their respective systems. Typically, there is easily enough energy imparted to the grains in a given tap to cause a grain to travel several grain diameters in a single tap, which would make the aforementioned methods of compaction unsuitable for particle tracking.

Fortunately, there is another more gentle method of compaction that does not impart kinetic energy to the grains during the compaction process. This process, known as thermal cycling, achieves compaction by slowly expanding and contracting the size of the grains or the surrounding container by controlled heating and cooling [1]. The grains and surrounding container have different thermal expansion coefficients (up to two orders of magnitude different), so the grains are able to settle downward irreversibly due to gravity as the container expands or beads shrink. In such an experiment, the bulk packing fraction has been shown to increase in a

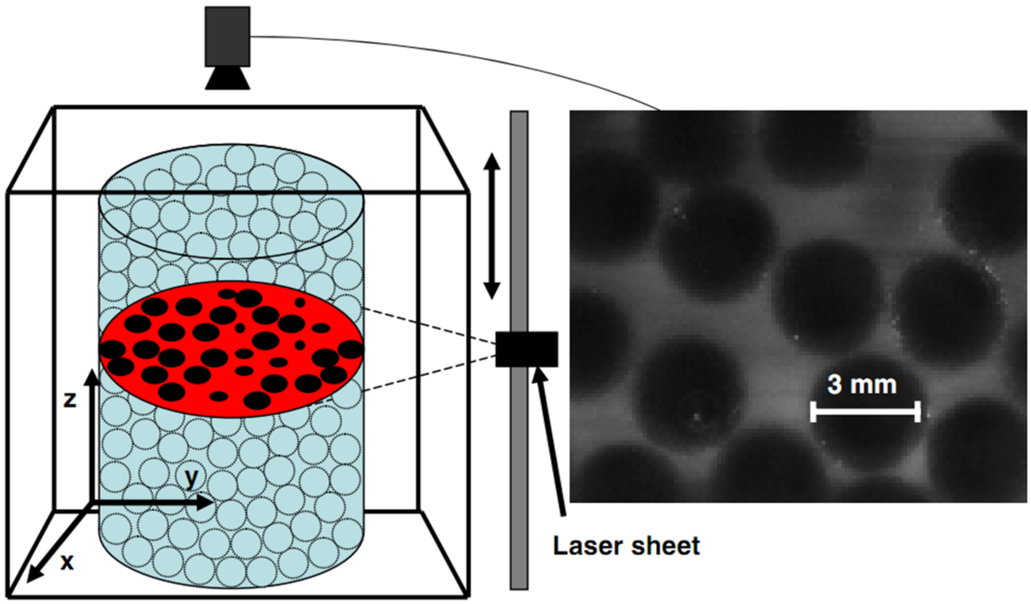

Figure 3.1: Schematic of thermal cycling setup

manner comparable to models of powders under tapping [1, 51]. Furthermore, it has been shown that the rate of compaction can be tuned by changing the temperature cycle ΔT. Thus, this method of compaction is ideal for study with the RIMS method.

3.2 RIMS Setup

We adapted the thermal cycling method from [1] for our imaging process (see Fig. 3.1). The granular material used is soda-lime glass beads (diameter D = 3 $\pm$ 0.3 mm), poured into a transparent polymethylpentene (PMP) cylinder of diameter

5 cm (16.6D) to a height of 19.5 $\pm$ 0.5 cm (63.3D to 66.6D, based on three different pourings). The thermal expansion coefficient for PMP is 1.17×10^{-4} K^{-1}, about 1 order of magnitude larger than that of the beads (9×10^{-6} K^{-1}) [1]. These were the same types of materials useds in previous thermal cycling measurements [1]. In order to apply the RIMS technique, we immerse the beads in an index-matching oil (Cargille Labs type DF) which contains 2.08 ug/ml laser dye (Nile Blue 690 perchlorate). The sample and oil are index-matched at room temperature. A transparent weight of 145.5 g was placed on top of the particles to monitor the filling height and to apply a controlled vertical force.

We developed a protocol to prepare the system for its initial loose packing state. We first pour the beads into the cylinder. We then fill the cylinder to the brim with our dyed index-match fluid, using a stirring rod to gently release any air bubbles trapped between the beads. Once the air bubbles are removed, we initialize the system by sealing the top of the cylinder, inverting it, and quickly righting it so that the beads settle to the bottom. We then drop our transparent weight into the cylinder, making sure that no air bubbles are trapped beneath it. Finally, we siphon the excess fluid from the top. This protocol ensures a loose packing, albeit with some variation in filling height for the same set of beads.

In order to achieve a level filling height, we place a transparent weight on top of the pile. This weight, formed to slide freely in the cylindrical container, provdes a constant downward pressure. It is immersed in the same index matched fluid as the beads, having the same density of the individual grains.

We use a transparent water bath to heat and cool the plastic vessel to induce compaction. The water in the tank may be heated or cooled at a rate of 16°C/hr. As the vessel is heated (cooled), the cross-sectional area expands (contracts) by 0.46mm^2 for every degree heated (cooled), compared to the sample bulk, which expands by less than 10% as much ($0.037\,\text{mm}^2$ for every degree heated (cooled)). Since the index of refraction changes with temperature differently for glass and oil, we can only image our sample at the end of each thermal cycle.

We apply ten thermal cycles for three different temperature differentials: 25, 40, and 60°C. Each experiment has a minimum temperature of 20°C. We were limited to ≈ 10 cycles because the heating caused the fluid to degrade so as to lose its transparency and refractive index matching at room temperature. Additionally, the laser dye becomes noticably fainter with each temperature cycle. This degradation makes long term 3D imaging impossible. Also, we were only able to measure the filling height for the experiment with $\Delta T = 60$°C, as the extreme high temperature (80°C) apparently degraded the fluid within a single cycle.

3.3 Results

3.3.1 Bulk Compaction

The filling height of the ensemble is determined from the vertical position of the flat glass weight on top of the pile in the 3D image, and the initial conditions are generated by letting particles settle into the oil-filled cylinder. The packing fraction was calculated by dividing the volume of the grains, determined from water displacement measurements, by the occupied volume of the cylinder, determined

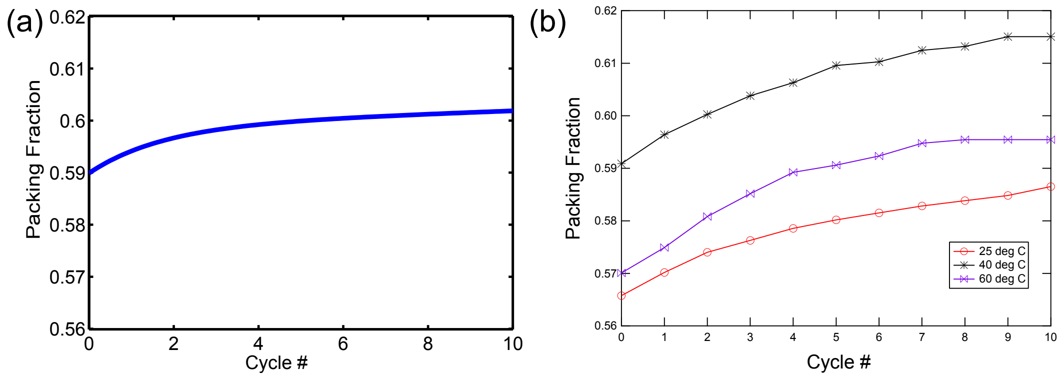

Figure 3.2: (a) Best fit curve to Schiffer data for a thermal cycling system with $\Delta T = 40°\text{C}$ (from supplemental information, [1])(b) Experimental data from filling height measurements of RIMS system for $\Delta T = 25$, 40, $60°C$. Note that the initial packing fraction varies with each experiment.

from filling height measurements. After the particles settle, the glass top is allowed to sink onto the surface of the fluid-immersed particles. Filling in oil first is necessary to eliminate air bubbles from the sample but leads to significant variability in the initial packing fraction. Nevertheless, the increase in packing fraction during thermal cycling can be fit with an exponential $\rho(n) = \rho_0 \left(1 - e^{n/n_0}\right)$ as shown in Fig. 3.2 . In all cases, the compaction rate $\frac{1}{n_0}$ is slower than the faster of two compaction rates found in a double exponential fit of thermal cycling compaction data for a dry system with similar materials [1] (supplemental material, $\rho = 0.64 - 0.01e^{-\frac{x}{2.7}} - 0.04e^{-\frac{x}{130}}$). We speculate that the rates of compaction differ between dry and fluid-immersed systems due to fluid-grain interactions, such as buoyant forces or lubrication between grain surfaces.

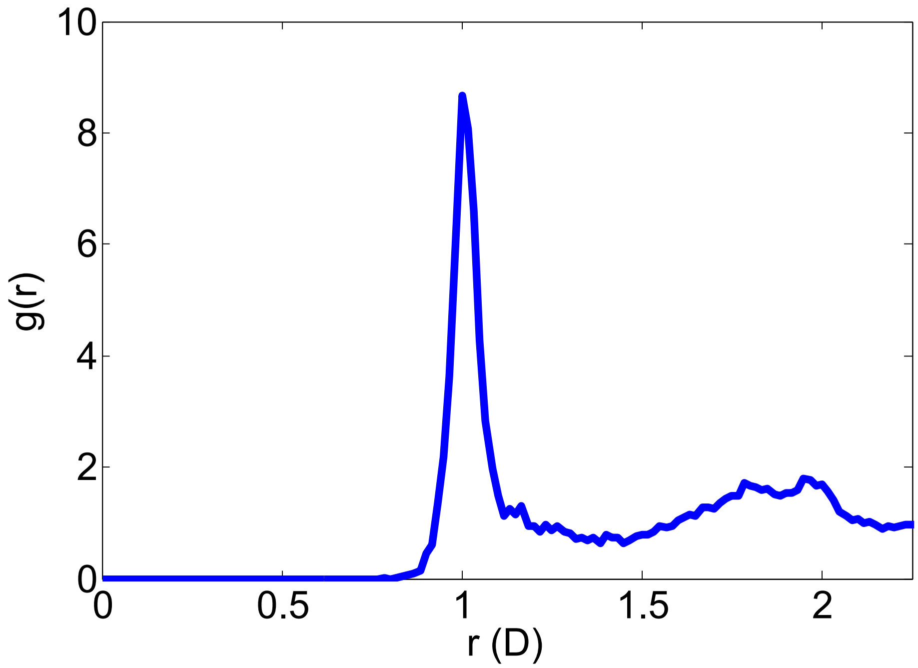

Figure 3.3: Typical Radial Distribution Function $g(r)$.

3.3.2 Pair Correlation Function

We test for changes in global ordering by calculating the pair correlation function g(r). The function g(r) is defined as the distribution of radial displacements of particles, normalized by the number fraction of particles expected in a spherical shell of size $4\pi r^2 dr$. This measure is known to have a sharp peak at the grain diameter that grows in dense systems of particles approaching packing fractions near 0.64 [52].

However, we find that, for our system, $g(r)$ does not evolve significantly from one temperature cycle to the next. A representative plot of $g(r)$ is shown in Fig. 3.3. This is not surprising since the particles need to move closer only by about 0.015D on average to achieve an increase in packing fraction of 1.5%. The overall shape of g(r) is consistent with a dense, random arrangement of particles, such as Lenard-Jones liquids [53].

3.3.3 Voronoi Volume

Since the compaction process involves minimizing the total volume of the system, we turn our attention to the local free volume available to each grain. We can partition the space of our granular ensemble based on the spatial distribution of grains, producing a local volume, known as the Voronoi volume (sometimes called Voronoi cell), about each centroid. The Voronoi volume is a well defined construct in Computational Geometry for a set of points in an $\Re^n$ space. In three dimensions, a Voronoi volume is a convex polyhedron that encompasses all the space that is closest to a given grain center. A schematic, showing the construction of a 2D analogous Voronoi area, is shown in Figure 3.4.

The Voronoi volume structures were determined using the Qhull algorithm [54]. We restrict our analysis of Voronoi neighbors to interior grains. Grain centers at the edge of our field of view tend to create a systematic bias in our neighbor analyses, since they either have fewer neighbors than average, such as grains on the top surface of our pile, or have missing neighbors, such as grains at or near the walls of the containing vessel. After we partition our space into Voronoi cells, we select Voronoi neighbors of grains with centers in a box region that is 1.5 grain diameters (greater/less) than the (minimum/maximum) grain center coordinate in the (x,y,z) dimension. Thus, the particles at the edges of our region of interest serve

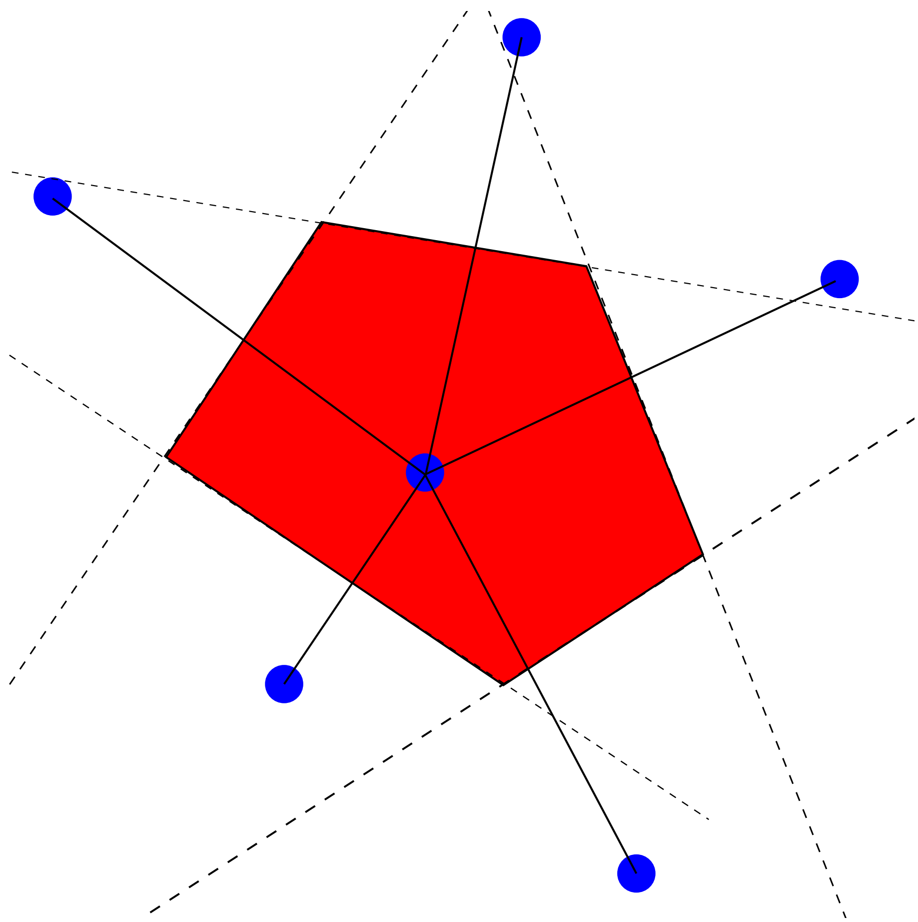

Figure 3.4: Example of a single Voronoi cell constructed about a point in 2 Dimensional space.

as boundary points for our Voronoi cell construction.

The distributions of Voronoi volumes are shown in Fig. 3.5. The distribution is non-Gaussian with a sharp cutoff at small volumes and a broad range of large volumes, similar to distributions observed in simulations in glass-forming liquids [55] and in recent experiments of granular materials [2].

One possible functional form of the distribution of Voronoi volumes proposed by Aste et al [2] contains only one fitting parameter k:

$$f(V,k) = \frac{k^k}{(k-1)!}\frac{(V-V_{min})^{(k-1)}}{(<V> - V_{min})^k}\exp\left(-k\frac{V-V_{min}}{<V> - V_{min}}\right) \tag{3.1}$$

This functional form, explained in detail in [56], is a consequence of the Edwards ensemble statistical mechanical analog of granular media [57], wherein volume is analogous to energy.

Fitting our Voronoi volume distributions to this function using an implementation of the Levenberg-Marquardt algorithm [58] yields k = 14.2 ± 0.6, which is close to the range of k values suggested by Aste et al [2]. We also find that the distribution of Aste et al is consistent within numerical uncertainty with the Voronoi volume distribution found in the recent molecular dynamics simulations of Starr et al. for a variety of cooled molecular liquids (polymeric, water, and silicon) [55]. Moreover, the Voronoi volume distribution does not change significantly as the system is compacted. Our observations thus provide further evidence of the universality of the Voronoi volume distribution of strongly interacting fluids.

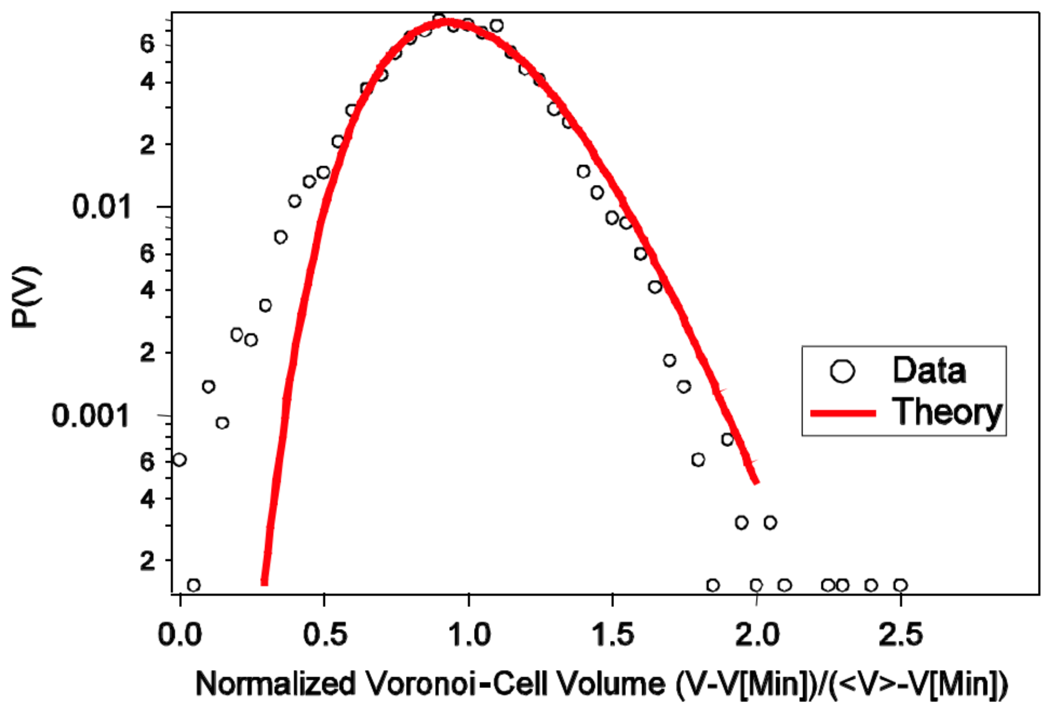

Figure 3.5: Distribution of Voronoi Cell Volumes Compared to the Theoretical Model by Aste et al. [2].

3.3.4 Voronoi Shape Vector

We also quantify the shape of Voronoi cells to measure correlations between the local free volume of grains and their subsequent displacements. In simulations of supercooled liquids, atomic motions were found to be strongly correlated with the orientation of the shape of the Voronoi cell [47]. We define the orientation of a Voronoi cell as a "shape vector" $\vec{u_{i,j}}$, which we calculate for each particle i prior to cycle j. This shape vector is the centroid of the outer vertices of the voronoi cell about particle i, taken with respect to the centroid of said particle, as shown in Fig. 3.6. Thus, the shape vector points to the "mean void" about particle i, since the vertices of all Voronoi cells correspond to the gaps between 4 or more grains in close contact.

In order to probe the dynamics of the grains, we compare their shape vetors at the start of a cycle to the subsequent displacements of the grains after said cycle. We define the vector $\vec{v_{i,j}}$ to be the displacement of the center of grain i from cycle j to $j+1$ (see Fig. 3.6). The averages for $|\vec{u}|$ and $|\vec{v}|$ are approximately 1 mm (0.33D) larger than the accuracy with which we detect grain positions. The magnitudes and directions of the two vectors were found to be uncorrelated to the volumes of their corresponding Voronoi cells.

We quantify the correlation between grain displacement and shape vectors by calculating the cosine of the angle between them. For each grain i in cycle j, we calculate $\cos\theta_{i,j}$ where $\cos\theta$ is determined as follows:

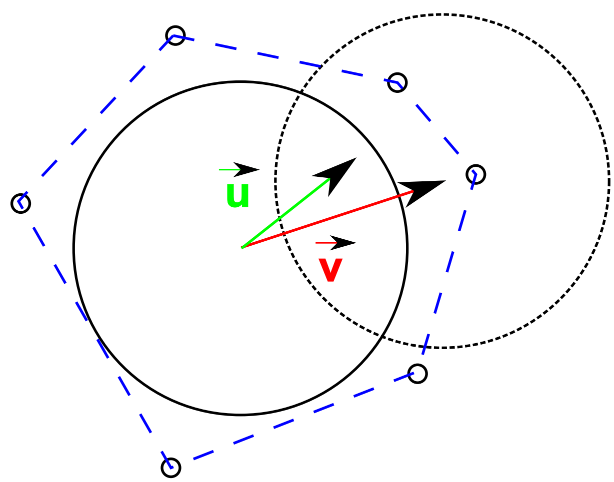

Figure 3.6: Schematic of Voronoi shape vector

$$\cos\theta_{i,j} = \frac{\vec{u_{i,j}} \cdot \vec{v_{i,j}}}{|\vec{u_{i,j}}||\vec{v_{i,j}}|} \tag{3.2}$$

The probability distribution of $\cos\theta$ averaged over all grains is shown in Fig. 3.7. In addition, we show the distribution for the first and the last cycles and a control for two 3D images without thermal cycling between the images. We find that the distribution peaks at $\cos\theta = 1$, indicating that the grain moves toward the center of the vertices of its Voronoi cell. Particle motion and Voronoi cell shape are indeed correlated. This correlation was found to be independent of either the size of the Voronoi cell volumes or the magnitudes of their corresponding displacement vectors.

3.4 Discussion

By using the laser sheet scanning method, we visualize the internal structure and dynamics of a jammed granular material. Under quasistatic forcing via thermal cycling, flows are slow enough (less than ≈ 0.5D between frames), so we can observe the microscopic dynamics of this strongly interacting grain system. While the differences in local structures are too small to be observable in local distributions such as g(r) or the Voronoi volume distribution, the Voronoi volume appears to hold important clues for the future dynamical evolution of the grains. Voronoi reconstruction indicates that grains tend to move toward the centers of Voronoi vertices as long ago observed in Rahman′s pioneering simulations of cooled liquids [47]. This correlated displacement in our granular fluid is independent of the size of the Voronoi volume,

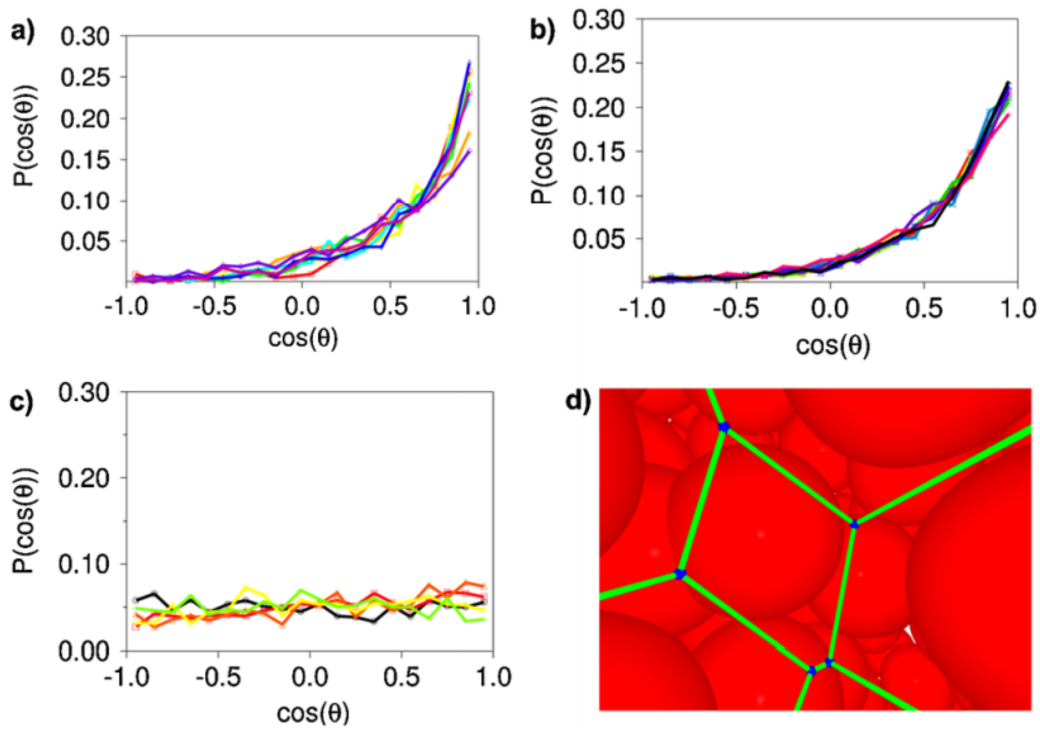

Figure 3.7: (a) Preferred direction probability distribution functions (PDFs) for a system with $\Delta T = 40$°C for each thermal cycle. (b) Preferred direction PDFs for a system with $\Delta T = 25$°C for each thermal cycle. (c) Preferred direction PDFs for a system at constant temperature. (d) 3D reconstruction of a system from the perspective of a given grain facing five vertices of its Voronoi cell. Notice that each vertex is located in the void between grains.

the velocity of grains, and the position of grains within the granular column.

Rahman [47] and others [59] inferred from the correlations in the tracer particle displacement and the Voronoi cell shape that the particles were moving in tubelike environments, suggesting the string-like motion in cooled liquids [60, 61]. This raises questions about whether such collective interparticle displacements also characterize particle motion in compactified granular materials. The absence of equilibrium in flowing granular ensembles, however, complicates the definition of mobile and collectively moving (i.e. string-like) particles in granular materials, since there is no model such as Brownian motion to provide a baseline for this comparison. Unfortunately, we cannot track particles long enough to perform a string analysis to connect the local collective dynamics with these large scale collective motions. However, studies of quasi-2D granular materials [62, 30] indicate the presence of collective string-like motion as in cooled liquids, so the general presence of such collective motions in driven granular media seems likely. The presence of such correlated motion implies the existence of correlations between shape fluctuations and particle displacements of adjacent Voronoi cells.

In future work, we could further investigate correlations between the displacement vectors describing the Voronoi cell-shape fluctuations to better understand the origin of collective string-like motion in strongly interacting fluids. Collective particle motion would appear as chain-like assemblies of particle displacement vectors, defining a collective coordinate for the string-like motion.

Chapter 4

Granular Dynamics in a Steady Shear Flow

In this chapter, we will discuss the split bottom shear cell geometry and its use in the study of slow granular shear flows. First we will discuss the unique advantages of the split-bottom geometry for the study of shear flows. Then we show how we adapt this geometry to the RIMS method in order to locate and track individual grains within the sheared bulk. Using these trajectories, we calculate various microscopic and mesoscopic quantities within the flowing region. To determine the rheology of our system, measurements of shear forces were carried out at Leiden University in collaboration with Martin Van Hecke's research group.

4.1 Split-Bottom Geometry

In order to observe shear flows, we employ a modification of the split-bottom geometry. This geometry, originally put forth by Van Hecke et al [63, 64], consists of a stationary container with a shearing disk of radius R_s recessed into the floor of a containing vessel, as in Figure 4.1. The surface of the floor of the vessel is generally made rough, either by digging pits in the surfaces or affixing grains to the surfaces, in order to reduce slippage between the bottom of the container and the grains.

The granular pile is poured into the container to a filling height H. The shearing disk is then rotated at a constant rate Ω. This induces a differential strain

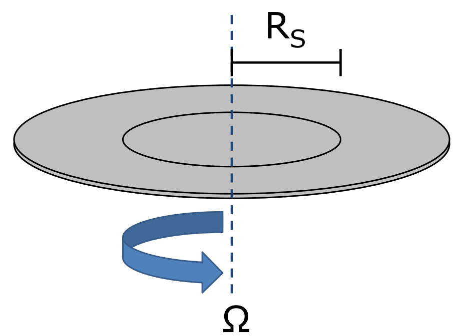

Figure 4.1: Basic Schematic of the split-bottom geometry. The inner disk, of radius R_s is rotated at a rate Ω. Cylindrical walls are not shown.

on the pile, which is resting on both the bottom surface of the cell as well as the shearing disk. The resulting flow pattern has a well-defined annular region of maximum shear that is essentially parallel to the shearing disk for small filling heights.

The flow patterns of this geometery have been studied extensively for several grain sizes, filling heights, and strain rates. The split-bottom shear flow pattern produces shear bands that are several grain diameters wide within the bulk of a given granular pile. For low filling heights of, typically $H/R_s < .5$, the angular velocity profiles with a high rate of differential strain yield shear bands that are on the order of 10 grain diameters wide (or 1.6 cm for beads of size 1.5-2 mm) and thicker [64]. For comparison, another typical shear geometery, the couette geometry (two rough concentric cylinders where the inner cylinder is rotating) has a shear profile that decays considerably within only 5.5 grain diameters of the moving boundary in the steady state [29]. Furthermore, for each axial cross-section of the system, the angular velocity profile $\omega(r)$ follows a universal curve:

$$\omega(r) = \omega_0 \left\{ 1/2 + \mathrm{erf}\left(\frac{r - R(z)}{W(z)} \right) \right\} \tag{4.1}$$

where R and W follow these relations [63, 65]:

$$(R_s - R(z))/R_s = (z/R_s)^{5/2} \tag{4.2}$$

$$W(z) = W_{(z=H)} \sqrt{1 - \left(1 - \frac{z}{H}\right)^2} \tag{4.3}$$

This annular profile does not persist for all filling heights though. When $H/R_s > 1$, the shear region takes on a cupolar (dome-like) shape that crosses over the axis of symmetry. The angular velocity profile about the axis of rotation decays with increasing height according to the empirical relation [3]:

$$\omega(z, r = 0)/\Omega = a + (1 - a)e^{-z^2/2\sigma^2} \tag{4.4}$$

where a is dependent upon the height of the pile, and σ is a fit parameter. A depiction of the shape of the flow profiles for various filling heights is shown in Figure 4.2. Thus, for high filling heights, the shear profile has a more complex flow profile.

In any case, it is worth noting that, except near the bottom, these shear regions occur several grain layers above the boundaries. This property makes the split-bottom geometry particuarly favorable for the study of dense shear flows, in that the shear flow gradient is not always near a boundary.

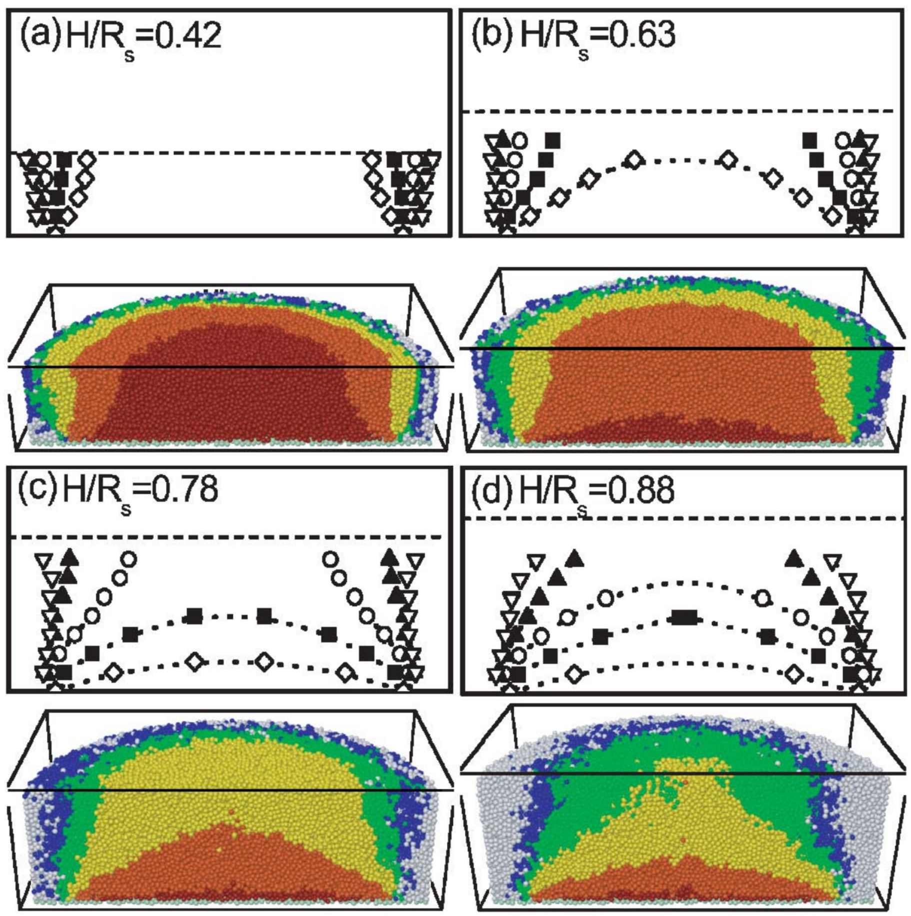

Figure 4.2: Shear flow profile reconstructions within a split bottom geometry for several filling heights, based on NMR imaging performed by [3] *Figure courtesy of Sid Nagel.*

4.2 Modified Split Bottom Geometry with RIMS

In order to probe the internal structure of a split-bottom induced shear flow with the RIMS method, we must make some modifications to the apparatus without significantly altering the characteristics of the bulk flow. Our first concern is to ensure that the laser sheet passes through the material without any lensing from the walls. This is achieved using a square box with transparent walls as an outer container, so that the light of the laser sheet is minimally distorted within each cross-section (Figure 4.3).

We choose a motor for our shearing disk that is able to make precise, slow rotations. Since we can only image our system slowly, we must minimize the amount of rotation between frames as well as the rate of rotation, either of which could potentially cause some of the grains to be displaced significantly more than its surrounding grains [66]. Our shearing disk is coupled to a servo motor (Pacific Scientific PMA 24C), via a planetary gear with a gearhead ratio of 25:1. The motor has an internal resolver that can resolve the position of the disk within 1 minute of arc (25 minutes of arc before the gearhead), as well as a velocity resolution of 0.000572 RPM (0.0143 RPM before the gearhead). Thus, we are able to make small, controlled ajustments to the position and speed of our shearing disk.

Next, we take steps to ensure that the essential physics of the split-bottom system are not lost when we adapt the system for RIMS imaging. In particular, we want to ensure that the shear flow profile of the grains is affected by neither the presense of interstitial fluid nor the square boundaries of the vessel. We must

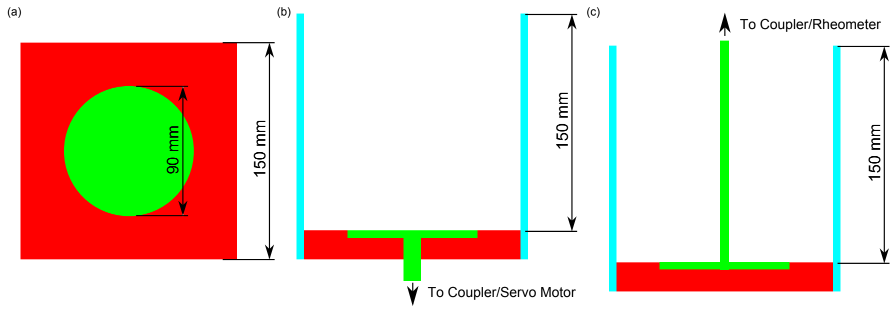

Figure 4.3: Schematic of Split Bottom Shear Cell Modified for RIMS imaging. (a) Overhead view of system drawn to scale. Note that the center of the shearing disk (green) coincides with the center of the floor (red) of the containing vessel. (b) An axial cross-section of the system showing how the shearing disk is recessed into the floor. A shaft joined to the disk is coupled to a servo motor. The walls (cyan) allow for the system to contain up to 3.375 L of fluid-immersed grains. Not shown: A lip seal at the top of the shaft that blocks fluid from leaving the vessel, and a roller bearing that allows the shaft to rotate freely. (c) An alternate configuration of the split bottom geometry for use with a rheometer. In this case, the rheometer is mounted above the system.

measure both the rheology and particle-level dynamics in order to test for this.

In work done in Leiden with contributions from Joshua Dijksman, Wlie Wandersman, and Chris Berardi, we verified the rheological properties of the system by attaching a rheometer (Anton Paar MCR 501) to the shearing disk. The disk is rotated for a wide range of rotation rates and filling heights of 3/16" PMMA beads while immersed in Triton X-100. We find that for rotation rates below 10 mrad/sec, the steady state torque is independent of the rotation rate of the shearing disk (Figure 4.4).

Furthermore, we see that the effective frictional coefficient for our fluid- immersed grains are similar to dry grain systems. A model for the split-bottom geometry for the height dependence of steady state torque on the shearing disk is given as follows:

$$T(H) = 2g\pi\rho\phi\mu_0 \int_H^0 (H-z)r^2\sqrt{1+(dr/dz)^2}dz \tag{4.5}$$

where g is the gravitational constant, ρ is the buoyancy-corrected density of the grains, ϕ is the packing fraction of the grains, and μ_0 is the effective friction coefficient of the grains. We find, using the torques in the quasistatic limit of the stress-strain rate relations in Figure 4.4a that Equation 4.5 fits the data best for the cases where $\mu_0 = 0.59 \pm 0.03$ for fluid-immersed grains, and $\mu_0 = 0.57 \pm 0.03$ for dry grains (see Figure 4.4b). This result, which is in agreement with previous obervations in immersed granular media [67], indicates that our interstitial fluid has a minimal effect on the physics of the granular flows, provided we conduct our experiments within the quasistatic regime. For rotation rates above 10^{-2} rev/sec, the system becomes rate dependent, with steady state stresses rising in a manner directly proportional to the shear rate.

4.3 Shear Zone Selection

Since we are primarily interested in the behavior of the grains within the shearing region, we want to focus our attention on this section of our system. We use the trajectories of the grains in a steady shear flow to construct a mean flow profile. We choose a cylindrical coordinate representation of the system centered about the axis of rotation of the disk. For a given washer-shaped sector of the system ($r \in (r_0, r_0+\Delta r)$, $z \in (z_0, z_0+\Delta z)$, we measure the mean azimuthal velocity $\omega(r,z)$

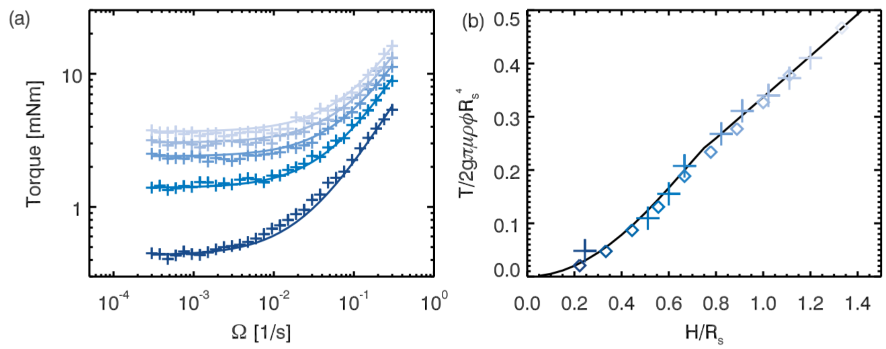

Figure 4.4: *Analysis in this figure was performed by Joshua Dijksman and is included here for reference.*(a) Rheology of 4.6 mm acrylic particles in pure Triton X-100. $T(\Omega)$ for a H/R_s = 0.24, 0.51, 0.60, 0.67, 0.82, 0.91, 1.0, 1.1, 1.2; color indicates H/R_s. $\Omega = 3.0 \times 10^{-4}$ to 0.3. The curve is a fit of the form $T = T_0 + C\Omega$. (b) $T_0(H)$, the plateau values as a function H compared to the prediction from Eq. 4.5 with $\mu = 0.57 \pm 0.03$ for the dry ($\diamond$) and $\mu = 0.59 \pm 0.03$ for the suspension (+) case.

of all grains in said sector for 6° of shear strain (3 consecutive frames). We find that there is a distinct locale within the differential azimuthal flow just above the shearing disk wherein both $\frac{\partial \omega}{\partial r}$ and $\frac{\partial \omega}{\partial z}$ are at a maximum. We call this region the "shear zone" due to the high differential strain.

We use the shape of our mean flow field to define bounds for our shear zone. As of this writing, there is no commonly accepted master flow field model, $\omega = f(r, z)$ for this system when $H/R_s \approx 1$, save for $\omega(r = 0, z)$ as noted above.

4.4 Dynamically Defined Nearest Neighbor Network

We use our trajectory data of our grains to form a Nearest Neighbor Network to represent our ensemble. A Nearest Neighbor Network is an undirected graph, where the grains are the vertices of the network and the edges represent (likely) contacts between pairs of grains. As the system evolves, the edges are added and deleted based on changes in the relative positions of grains. This Nearest Neighbor Network allows us to observe topological changes in our ensemble.

In order to constuct a Nearest Neighbor Network that is faithful to the structure of our ensemble, we must be precise in our determination of nearest neighbors. One limitation of our image analysis technique is that we are unable to determine whether or not a given pair of nearby grains are truly in contact with one another. The beads we use typically have a tolerance of $\approx 5\%$, so the radii of all grains are not strictly identical. Furthermore, since the spatial resolution of our images is typically ≈ 100 microns per pixel, particles that are as far as 50 microns apart could appear to be in contact. This is a general shortcoming of visual determination of contact, as a pair of grains could be several orders of magnitude closer to each than our resolution limit and still not be in contact or carry mechanical forces. Thus, we can only consider whether or not particles are likely in contact based on their relative proximity.

We select a proximity criterion based on the dynamical behavior of grains near neighbors. We observe that grains in a dense ensemble tend to preferentially roll or slide past their neighbors when subjected to a force. We use this constraint on grain dynamics to infer a criterion for proximity.

4.4.1 Model: Dense Soft Sphere ensemble

In order to determine how close two grains must be in order to be considered "in contact," we consider results of simulations of dense disordered packings. One model for densely packed particles is the "soft sphere" model [68, 69], which we have described in detail in Section 1.4.1.

We employ a statistical measure introduced by Ellenbroek et al [41]. In their simulations of dense disordered packings, they sought a measure of the prevalence of "floppy modes," wherein the particles in their systems respond to small stresses by moving perpendicular to their relative bond orientation, as this motion is more energetically favorable.

In this work, Ellenbroek et al determine which pairs of particles were rolling or sliding past one another based on an angle, α between the bond orientation vector of the centers of two neighboring grains and the relative displacement vector (see Figure 4.5).

Ellenbroek et al show that, for small perturbations of densely packed particles, the distribution of α angles has a Lorentzian shape with a peak about $\alpha = \pi/2$, indicating a strong preference for rolling/sliding behavior. This behavior has been observed in physical systems such as 2D foams [70], as well as in 3D granular flows [71]. Here we simply use the observation that the distribution of α angles has a peak for grains that are in contact, yet are forced to move.

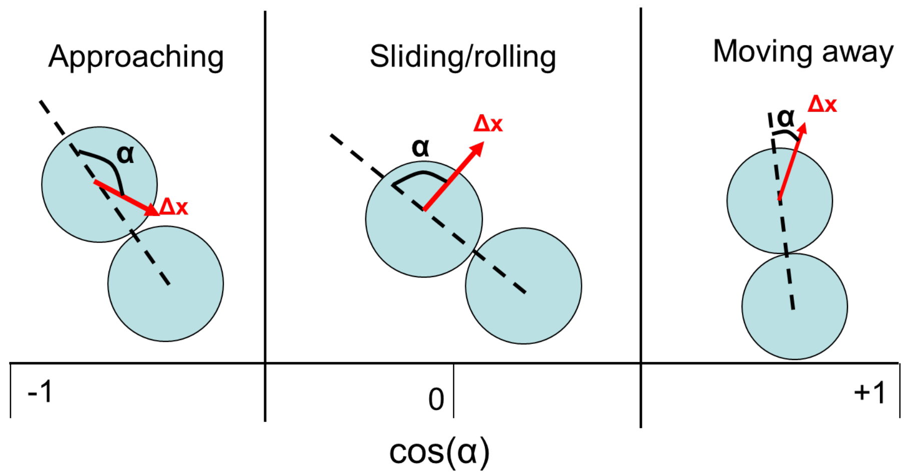

Figure 4.5: Schematic of alpha angle measure. Three major modes of relative motion: approaching, rolling/sliding, and separating, are associated with $\cos\alpha$ values of approximately -1, 0, and 1, respectively.

4.4.2 Analysis

We begin with a simple assumption regarding the alpha angle: the preference for rolling/sliding behavior is observed if and only if the pairs of grains are close enough to be in contact. We use the trajectories from our steady sheared system to find the distribution of α angles for grains at various initial distances from one another. In this test system, the grains typically move ≈ 0.3D between 3D scans.

We select pairs of particles that start out roughly 1.6 D apart or less from one another. We choose one grain from each pair to be the point of reference, calculating the relative displacement of the second grain after 3 frames of displacement, or 6° of system strain. We use this displacement interval to ensure that mean grain displacements are well above the resolution limit of our imaging system.

We then calculate $\cos\alpha$ between the radial separation vector of the grains and

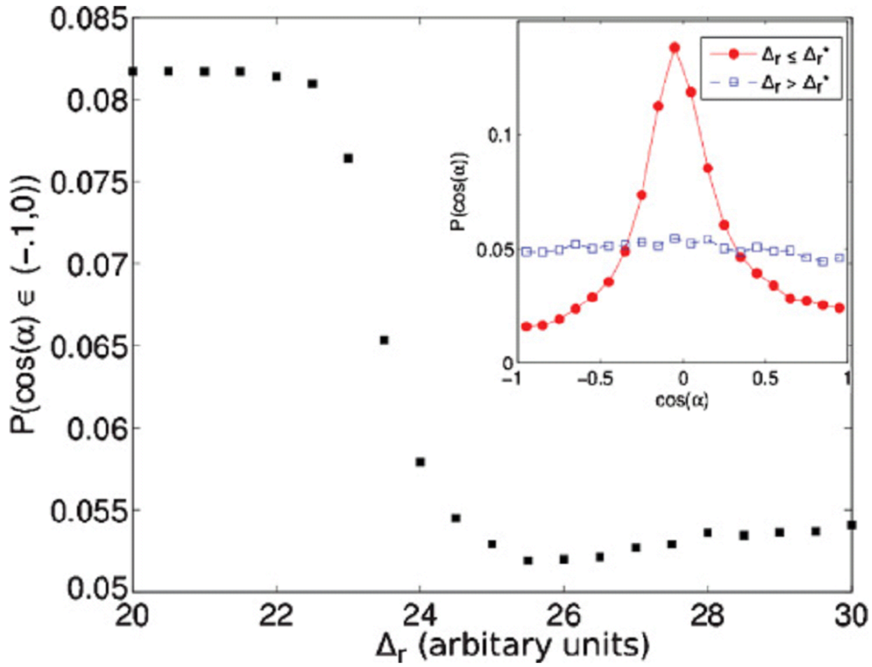

Figure 4.6: The peak value of the a cosines, $P(\cos\alpha)$ as a function of radial displacement Δ_r, where Δ_r is measured in an arbitrary scale. Smaller peak values indicate more uniform distributions. Note the sudden decrease to uniformity as the radial displacement increases. We take the value after the sudden decrease ($\Delta_r^* = 24.5$ in this case) as our conservative upper bound on particle contact distance. Inset: The distribution of $P(\cos\alpha)$ for touching $\Delta_r < 24.5$ (circles) and nontouching $\Delta_r > 24.5$ (squares) particles.

the relative displacement vector of the second grain for all pairs of nearby grains. Once the $\cos\alpha$ values are calculated, we compile a histogram, $P(\cos\alpha)$, of the results. We note that for grains whose centers are close to 1 grain diameter apart, $P(\cos\alpha)$ has a Lorenzian shape (see circle plot in Inset of Figure 4.6), consisent with previous experimental and theoretical results [41, 70].

The Lorenzian shape of $P(\cos\alpha)$ that we find does not hold for grains that are too far apart. For instance, when we only consider pairs of grains with centers spaced 1.2 to 1.3 grains appart, we find $P(\cos\alpha)$ to be more uniform (see square plot in Inset of Figure 4.6). This suggests that the bias for perpendicular displacements is a phenomenon dependent upon whether or not grain pairs are likely in contact.

We can use this local rolling/sliding result to determine an appropriate cutoff Δ_r^* for nearest neighbors. To do this, we calculate $\cos\alpha$ for grains whose centers are around 1 to 1.7 grain diameters apart. We then calculate $P(\cos\alpha)$ for all grains that are between Δ_r and 1.7 grain diameters apart, for several values of Δ_r. We define the peak of $P(\cos\alpha)$ as the fraction of cosines between -0.05 and +0.05. When we plot the peak in $P(\cos\alpha)$ versus Δ_r (Figure 4.6), we find a sudden decrease in the peak for grains that are separated beyond a threshold value of Δ_r. We choose this threshold Δ_r as our maximum separation criterion Δ_r^* for the selection of nearest neighbors. Note that this definition is purely based on collective grain dynamics, with no a priori knowledge of grain sizes required.

4.4.3 Alternate Method: Voronoi Analysis

An alternate method for choosing nearest neighbors is by using the Voronoi cells of the grains, as previously described in Section 3.3.3. If the Voronoi cells of two grain centers share a common facet, those grains are said to be Voronoi neighbors. An example of neighbors based on the Voronoi cell construction is shown in Figure 3.4.

This definition has some advantages. Since this criterion only requires the knowledge of the center position of grains, it also may be applied to a given system without explicit knowledge of the size of the grains. Thus, this nearest neighbor criterion may also be extended to systems with multiple grain sizes, or even non-sperical shapes, provided that the centroids of the grains are known. Also, unlike the aforementioned criterion for nearest neighbors, the Voronoi neighbors can be determined for single static frames. In short, the Voronoi neighbor criterion is both a simple and versatile criterion of determining neighbors of grains. However, it yields roughly twice as many nieghbors on average (≈ 12) in 3D compared to the previous neighbor definition (≈ 6).

However, the Voronoi volume nearest neighbor criterion does have some disadvantages. The major drawback is that under certain circumstances, such as when there are large gaps or lost grain centers, a pair of grains that are visibly separate may still be considered "nearest neighbors." Furthermore, when two grains of different sizes are in contact, their common facet passes through the larger grain, misrepresenting the actual location of the contact point. Thus, without some consideration for experimental errors or polydispersity of grains, the Voronoi volume criterion for nearest neighbors leads to a systematic overestimate of nearest neighbors and disregards the location of potential contact points.

4.5 Bond Orientation

We can use our nearest neighbor network to determine the short range order of the ensemble using the bond orientation parameter Q_6. This parameter, first introduced by Steinhardt et al [45], tells us about how particles are arranged relative to their nearest neighbors. It is defined for a given particle as follows:

$$Q_6 \equiv \sum_{i=1}^{N} \left\{ \frac{4\pi}{13} \sum_{m=-6}^{m=6} \left| \langle Y_{6m} \left[\Theta(\vec{r}_i), \Phi(\vec{r}_i) \right] \rangle \right|^2 \right\}^{1/2} \tag{4.6}$$

where N is the number of neighbors a given particle has, $\vec{r}_i$ is the displacement from the center of the given particle to one of its neighbors (in spherical coordinates), and $Y_{6m}(\theta, \phi)$ is the spherical harmonic function of order $l = 6$. Generally, the number Q_6, which typically falls between 0 and 1, indicates how structured the bonds between neighboring particles are. Some examples of Q_6 for highly symmetric structures include 0.57 for face-centered cubic configurations, 0.48 for hexagonal close-packed configurations, and 0.66 for icosahedral configurations.

Recently, it has been shown that for disordered packings of granular materials with packing fractions of ≈ 0.60, the average Q_6 value of a given grain, using the Voronoi neighbor definition, is ≈ 0.33 [72] for grains with 14 neighbors on average, which is significantly lower than for systems with crystalline ordering. This result is in agreement with observations of spatially uncorrelated hard sphere systems as defined in [73], where the mean value of Q_6 is shown to be proportional to the inverse square root of the number of contacts.

Using our nearest neighbor network to determine which pairs of grains form bonds, we find a mean Q_6 value of roughly 0.48. Using this information, the data from [72], and the relationship from [73], we see that the effective number of contacts is 6 to 7 on average. This result is consistent with a hard sphere system that does not have high spatial correlations. Thus, we see that our system does not become spatially ordered when subject to steady shearing.

4.6 Fracture Dynamics

The analysis in this section was performed by Mark Herrera and Shane McCarthy. It is shown here to demonstrate how the Network of Nearest Neighbors calculated in Section 5.5 can be used to gain insight into collective dynamics.

We now use our Nearest Neighbor Network construction to quantify restructuring of a granular ensemble in a shear process. We define a secondary network, known as the Broken Link Network, to represent rearrangements in our ensemble. The Broken Link Network uses the same vertices as the vertices of our Nearest Neighbor Network. An edge is formed when an edge in the Nearest Neighbor Network that existed in an initial reference frame is removed. This edge is only removed from the Broken Link Network if that edge is re-introduced in the Nearest Neighbor Network.

We compare the behavior of the Broken Link Network to the percolation of a random network. One noteable property of random networks is the sudden formation of system-spanning connected components [74, 75]. A component is a subset of vertices in a graph wherein all vertices are connected to one another by a sequence of edges in said graph. In such a system, a phase transition is observed over multiple random networks, where the order parameter is the fraction of vertices in the largest component, called the Giant Component.

We observe a similar phase transition in our Broken Link Network as we shear

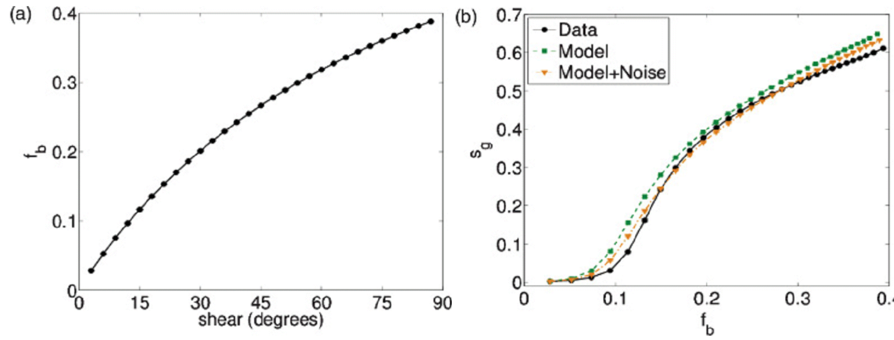

Figure 4.7: Growth of Giant Component in a steady shear process. (a) Increase of fraction of links broken f_b of the initial nearest neighbor network with increasing system strain. (b) Growth of Giant Component vs. f_b. Empirical data is consistent with models where the links are either broken randomly (Model + Noise) or weighted to preferentially break in regions of higher differential strain (Model).

the system. After roughly 20° of strain, the Giant Component grows abruptly, indicating system-spanning local rearrangements, despite a comparatively gradual increase in links broken over the same amount of strain (Figure 4.7). We note that these results are qualitatively consistent with models with random breakage events or breakage events weighted by local differential strain.

4.7 Conclusions

We see that our RIMS modifications do not interfere with essential physics of the split bottom geometry. Torque and PTV shear zone data indicate that, at slow shear rates, both dry and fluid-immersed systems behave in the same way.

At the grain level, we see that the system is quite disordered at the grain level. Trajectories of neighboring particles show a tendency of grains to roll or slide past their neighbors, with no apparent spatial ordering observed in 2 full revolutions of the shearing disk. Furthermore, we see that after only $\approx 20^\circ$ of strain, nearly 25% of all grains have at least one neighbor that has been changed.

There are several other measurements that could be taken in this system for future research. For instance, the Voronoi Shape Vector analysis could provide useful insight into the local motions of grains in the shear zone. It was not done in this experiment as the Voronoi construction is sensitive to a small number of missing grain centroids, which we did not explicitly correct for in this experiment. Furthermore, this system could be useful for measuring shear-induced segregation given the disordered nature of the system on short time scales.

Chapter 5

Cyclic Shear

This chapter is adapted from a publication by Slotterback, et al, [76] In this work, I performed all of the data acquisition, image analysis, and trajectory analysis, with the exception of the calculations involving the Giant Component Analysis.

5.1 Overview

In the previous chapter, we considered the flow of dense granular matter subject to quasistatic shear in a split bottom geometry. We now turn our attention to systems in which the strain direction is reversed, and cycled back and forth. We probe the microscopic and mesoscopic properties of the grain motions with respect to their neighbors. We show that there is evidence for a transient mode of motion wherein the flow pattern in a given direction is broken and reformed. Unless otherwise mentioned, we analyze trajectories that begin in the shear zone, as defined in secion 4.3.

5.2 Initial Torque Analysis

The data in this section were taken by William Derek Updegraff II using equipment in the lab of Martin Van Hecke at Leiden University.

We first assess the reversibility of our granular pile by probing the stress-strain behavior of our model granular medium upon reversal of shear strain. We use the split-bottom shear cell with the rheometer attached to the shearing disk (Figure 4.3c, shown again in Figure 5.1a). We prepared the system by preshearing the system, rotating the shearing disk several revolutions. We then rotated the shearing disk 15° in the same direction as the preshear at a rate of 5.2 mrad/sec, taking torque and angular displacement measurements at 0.1 sec intervals. After pausing for two minutes, we reversed the rotation of the shearing disk to 15° in the opposite direction as the preshear at a rate of -5.2 mrad/sec, taking torque and angular displacement measurements at 0.1 sec intervals (Figure 5.1b).

We find that there is a sudden qualitative change in rheological behavior at the onset of shear reversal. The torque required to reverse the direction of the shearing disk is initially negligible compared to the steady state torque required to keep the disk spinning at a constant rate. On the other hand, if the shearing disk is rotated in the same direction of prior shear, the torque on the disk reaches the steady state after only a comparatively miniscule amount of strain. This transient drop in torque at the onset of reversal in the split-bottom geometry has also been observed in reversal events of granular media in a Couette geometry [29]. When we fit the reversal torque curve to an exponential function of angular displacement, we find a characteristic strain of $4.9° \pm 0.2°$, which corresponds to 0.8 grain diameters of displacement at the edge of the shearing disk.

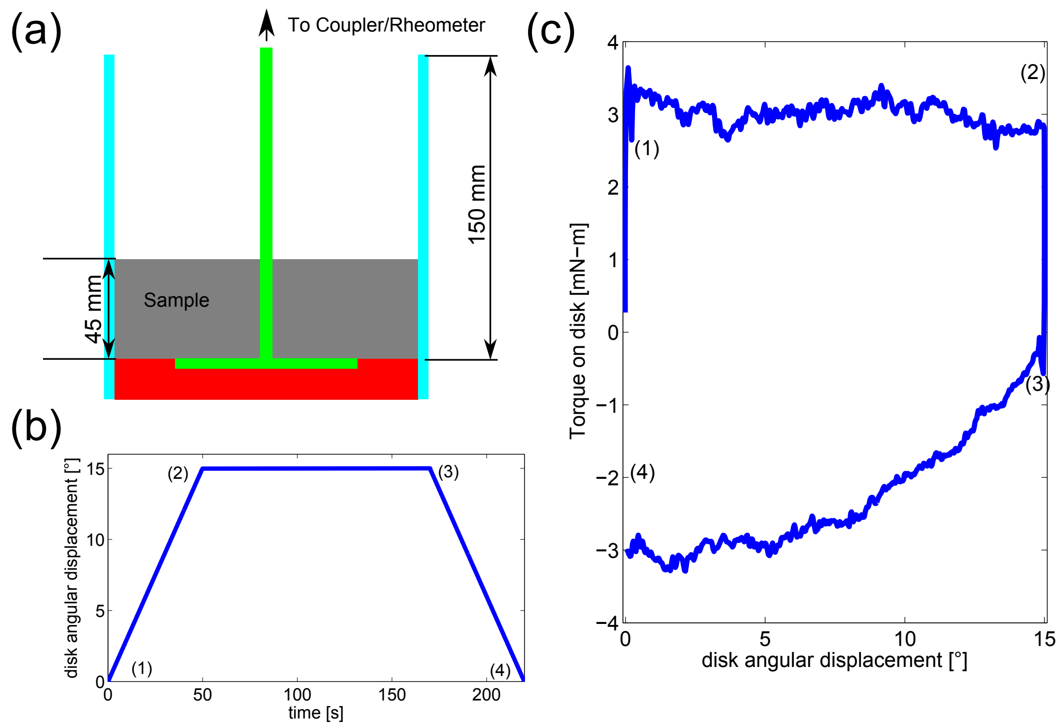

Figure 5.1: Shear Reversal Torque Experiment (a) Setup of apparatus with a rheometer attached to the disk. (b) Disk angular displacement as a function of time. (c) Torque on disk vs. disk angular displacement for three separate trials. A sequence of four data points is highlighted in both (b) and (c) to indicate the flow of time in (c).

5.3 Cyclic Shear Protocol

To create reproducible initial conditions representative of steady shear, we rotate the disk two full revolutions at 1 mrad/sec. At this rate of strain, the granular flow in our fluid immersed system is independent of strain rate, with the same velocity profile as a dry granular flow [77]. We then reverse the direction of rotation of the disk and move the disk for a strain of θ_r $(= 2°, 4°, 10°, 20°, 40°)$. We reverse the direction again and rotate the disk by $-\theta_r$ to its original position, thus straining and reversing the system in a cyclic fashion. We shear the system in 2° increments as noted in Figure 5.2, scanning after every 2° of strain. We perform 20 successive strain cycles in each experiment.

We do not observe a significant change in filling height within the 20 cycles of cyclic shear. This is consistent with filling height measurements of a similar split-bottom shear cell under cyclic shear, wherein the filling height (and, by construction, its packing fraction) changes by less than 0.2% over more than 100 cycles of shear at an amplitude of 2.1° and shear rate of 0.02 rev/sec. [78]

5.4 CMSD trends

There are many important quantities that we are able to calculate once we have the trajectories of all of the grains. One particularly useful metric for ensemble behavior is the Cumulative Mean Square Displacement (CMSD). The CMSD is a measure of how far on average grains move from their initial positions. It is slightly different from the traditional Mean Square Displacement (MSD) in that all

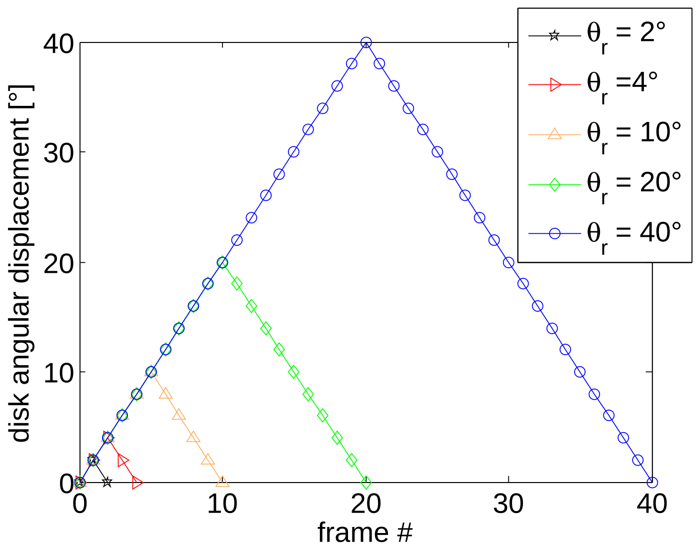

Figure 5.2: Applied Strain for 1 cycle of shear for six different values of θ_r. Note that the number of frames captured for 1 cycle is equal to $1 + \theta_r/2$

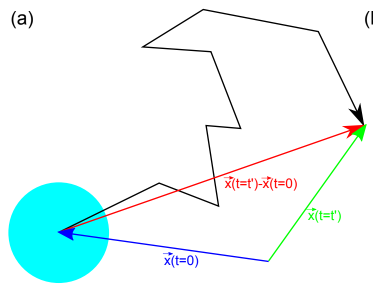

(b)

x (D)	y (D)	t (frame)
-2.47692	0.35384	0
-1.24460	0.93076	1
-0.58848	0.65768	2
-0.73460	1.61152	3
-0.31924	1.58076	4
-0.68076	2.50000	5
-1.48460	2.54232	6
-0.76152	3.00000	7
0.60768	2.73460	8
1.15000	1.63460	9

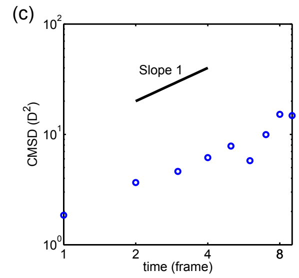

Figure 5.3: (a) Illustration a possible trajectory of a grain in 2D. Notice that the initial position does not necessarily coincide with the origin of the coordinate system. (b) The trajectory data, with position in units of grain diameters and time in arbitrary units. (c) A log-log plot of CMSD of given grain. A line of slope one is included for reference, indicating a typical trend for a diffusive system of particles.

displacements are calculated with respect to a single reference frame.

The CMSD ($\langle \Delta x^2 \rangle (t)$) is calculated as follows:

$$\left\langle \Delta x^2 \right\rangle (t) \equiv \frac{1}{N} \sum_{i=1}^{N} \left| \vec{x_i}(t) - \vec{x_i}(0) \right|^2 \tag{5.1}$$

where N is the number of grains, and $\vec{x_i}(t)$ is the position of the ith grain at time t.

An illustration of the CMSD for a single grain is shown in Figure 5.3a. Notice that the slope of the CMSD for this grain on a log-log scale, which we will call α, is close to 1 (Figure 5.3c). This indicates that the grain is following a roughly diffusive, as $\langle x^2 \rangle \approx t^\alpha = t$, which is not unlike a particle in a fluid undergoing Brownian motion [79].

Since we have the 3D trajectories of all of the grains, we could observe trends in the CMSD to characterize the motion of the grains by comparing the trend to a power law $\langle x^2 \rangle \approx t^\alpha$. Some typical trends are as follows:

- $\alpha = 0 \Rightarrow$ no motion at given time interval
- $0 < \alpha < 1 \Rightarrow$ sub-diffusive motion at given time interval
- $\alpha = 1 \Rightarrow$ motion consistent with diffusive behavior $x \propto \sqrt{t}$
- $1 < \alpha < 2 \Rightarrow$ super-diffusive behavior
- $\alpha = 2 \Rightarrow$ overall ballistic motion ($x = vt$).

5.4.1 CMSD along principal axes

Since we are shearing the system in the quasistatic regime, we plot the CMSD as a function of absolute strain (forward or reversed) imparted by the shearing disk with respect to an initial frame, rather than explicitly plotting as a function of time. (See Figure 5.4a).

We can calculate the CMSD along the principal axes. We assume a cylindrical coordinate system, with the axial direction parallel to the axis of rotation of the shearing disk. We note that the tangential component of the CMSD oscillates in phase with the shearing disk (Figure 5.4c). The radial and axial components of the CMSD grow roughly linear with the absolute amount of strain, reaching the same order of magnitude of CMSD after 20 cycles of strain of each strain amplitude (Figure 5.4b,d). Furthermore, after each full strain cycle, the tangential CMSD is at the same order of magnitude as the radial and axial CMSD components. This behavior suggests a superposition of reversible motion in the tangential direction,

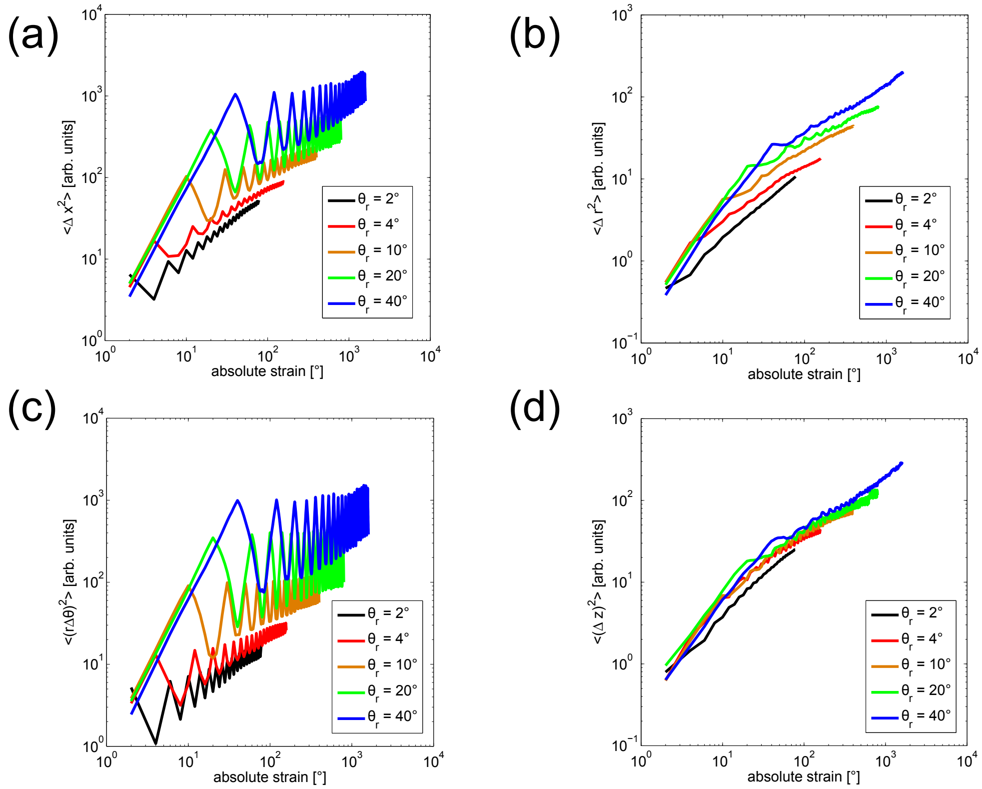

Figure 5.4: (a) Cumulative Mean Square Displacements (CMSD) Under Shear Reversal vs. absolute strain, for all values of θ_r. (b)-(d) Principal Components of CMSDs with respect to disk axis. (b) Radial CMSD, (c) Tangential CMSD, (d) axial CMSD. Note that the vertical axes on plots (b) and (d) are shifted one order of magnitude below those of (a) and (c).

along with diffusive, irreversible motion equally in all three spatial dimensions.

5.4.2 CMSD as measure of reversibility

Since the total CMSD after a full cycle is independent of choice of axis, we may also use the cycle-to-cycle CMSD values to measure how reversible the ensemble is. The CMSD of the grains in the shear zone at the end of each of the 20 cycles are shown as function of cycle number, n_c, in Fig. 5.5a. For all but the largest reversal amplitude θ_r, the slope of the CMSD decreases below 1 with increasing cycle number signalling slightly sub-diffusive motion overall.

To explore whether the system becomes more reversible after several shear cycles, we choose the beginning frame of a later starting cycle n_s as a reference frame. Fig. 5.5b illustrates that for $n_s = 10$, the CMSD is up to an order of magnitude smaller, suggesting that bead positions in this cyclic shear flow become more reversible after several cycles. Strikingly, the CMSD for the largest reversal amplitude ($\theta_r = 40°$) is considerably larger in magnitude, maintaining a comparable order of magnitude regardless of the number of preceding strain cycles.

To compare the rearrangements after one cycle of amplitude θ_r with two cycles of amplitude $\theta_r/2$ etc, we calculate the CMSD after a fixed absolute strain $\Delta\theta$ (relative to a chosen reference frame) which we fix here at 80° (a different number of starting cyles for each strain amplitude). Fig. 5.5c shows the CMSD at this fixed total strain as function of the start cycle n_s. We see that for $\theta_r = 40°$, the magnitude of the MSD does not depend strongly on the choice of reference cycle

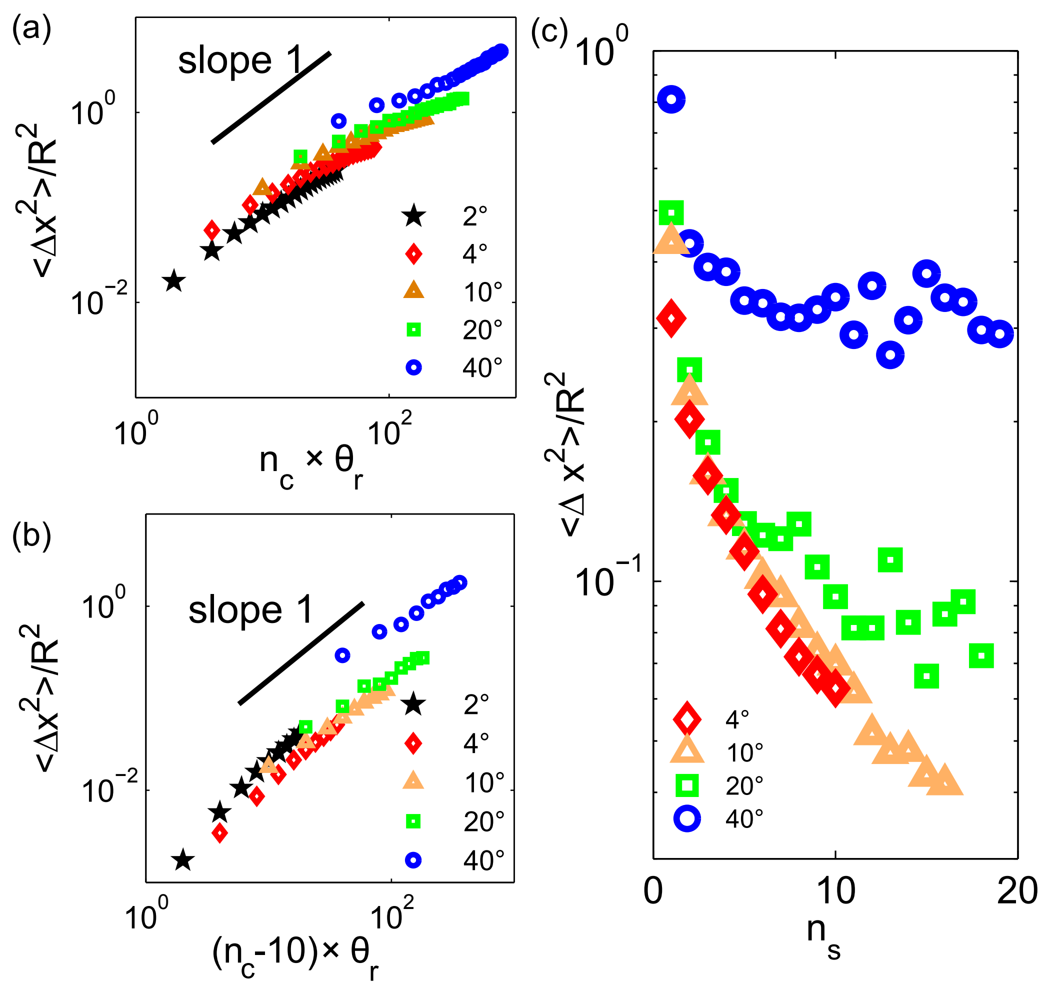

Figure 5.5: (a)-(b)Cumulative Mean Square Displacements (CMSDs) at the end of each cycle as a function of cycle number for different cycle amplitudes, scaled by the effective bead radius R: (a) Reference frame at the start of the first cycle, (b) The start of the 10th cycle is chosen as a reference frame. (c) CMSD after 80° of absolute strain vs. reference cycle number.

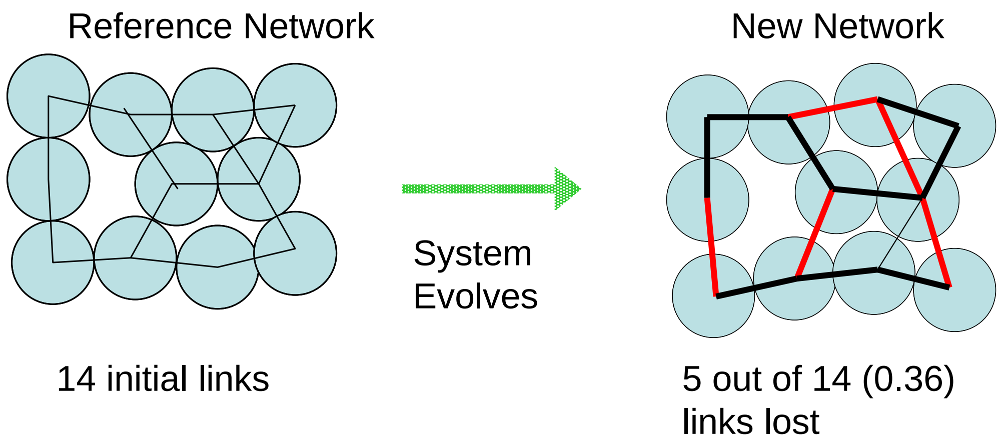

Figure 5.6: Schematic of f_b metric

after a short transient of about 3 cycles, while the MSD for smaller θ_r continue a downward trend for all cycles investigated. This indicates that the cyclic shear becomes more spatially reversible for strain amplitudes of 20° or lower, but not for strain amplitudes of 40° (or higher, most likely).

All three probes of the CMSD strongly suggest a qualitative change in behavior between $\theta_r = 20°$ and $\theta_r = 40°$: for large amplitude, the motion is irreversible, and reaches a steady, diffusive state, while for small amplitudes, the cyclic shear strain process becomes increasingly reversible and the system is aging.

5.5 Nearest Neighbor loss trends

As a second measure of reversibility we probe the network of nearest neighbors. We first identify all neighbors in a reference frame at the start of a cycle, using the nearest neighbor network defined in Chapter 4. Then we calculate, as function of frame number, the fraction of links broken f_b, defined as the fraction of neighbor pairs from the reference frame that are no longer within the cutoff distance used to define neighbors, as in the example networks shown in Figure 5.6. The approach of [71] has been modified here to include the possibility of "healing," which is the removal of a broken link when a neighbor pair from the reference frame reforms after being broken in an intermediate frame. Note that other pairs of beads may become neighbors in later frames but this is not considered in the broken link analysis.

In Figure 5.7a we show the evolution of f_b as a function of $\Delta\theta$, for $\theta_r = 10°$. Other θ_r show comparable results (see Figure 5.8). The top curve shows f_b with n_s=1. We observe a strong decrease in f_b when the strain direction is reversed (at 10°), indicating that broken links reform after reversal. Additionally, fewer additional links are broken in each subsequent cycle, suggesting that the motion becomes less irreversible for later times. The ten lower curves in Fig. 5.7a show f_b when the start of a later cycle is chosen as a reference frame, illustrating that the recovery of neighbors after a full shear strain cycle (at arrow) improves with increasing cycle number.

In Fig. 5.7b we show f_b after one cycle as a function of the starting cycle n_s, which provides a local measure of the reversibility of the configuration after one cycle. Clearly, the fraction of links broken decreases with increasing n_s (indicating an increase in reversibility) for all but the largest reversal amplitude, which appears to level off. As a simple local metric, f_b captures what fraction of the neighbor network is evolving with strain, a topological analog to the "particle activity" of

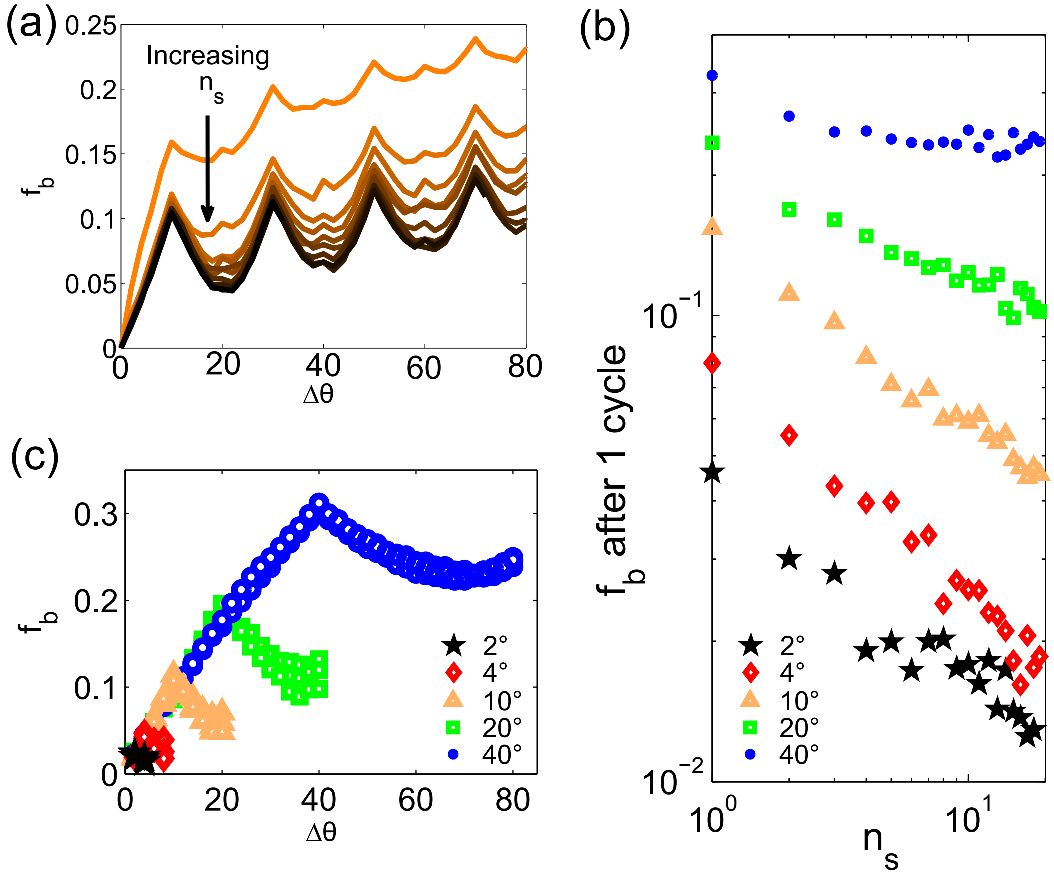

Figure 5.7: (a) Fraction of links broken, f_b for shear reversal vs. 2° strain step for the case of $\theta_r = 10°$. (b) f_b after one cycle as a function of the starting cycle n_s, for all θ_r. (c) f_b as a function of $\Delta\theta$ for representative curves at n_s=5, 10 and 15.

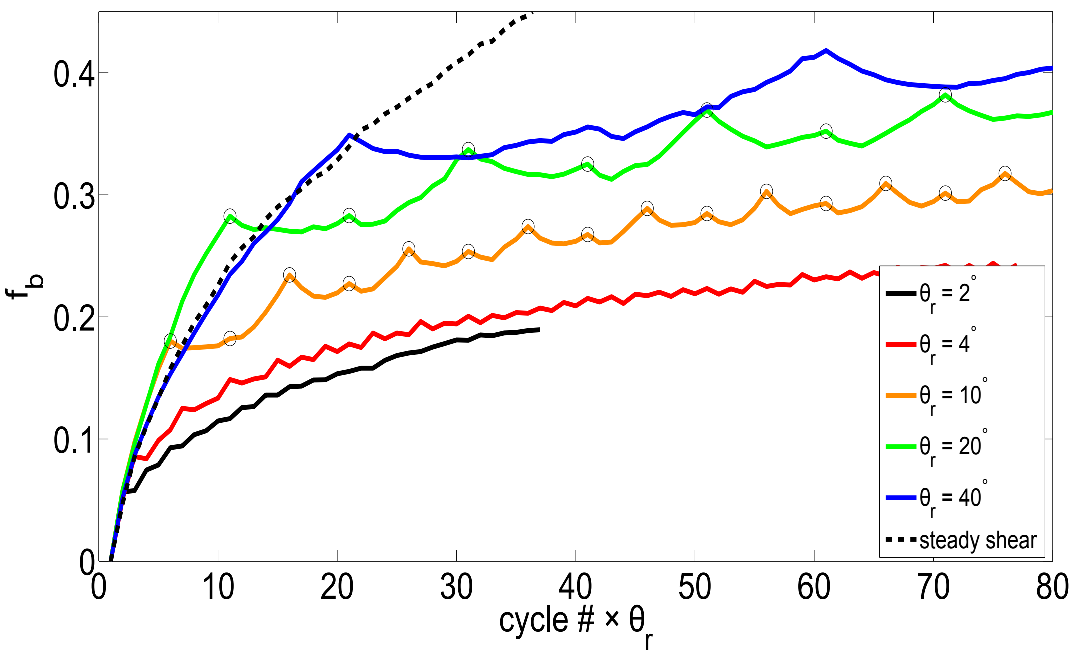

Figure 5.8: Trends in f_b for all θ_r and for steady shear case. Strain reversal events are highlighted with circles along the f_b trends for $\theta_r = 10°$ and $20°$.

[80]. Indeed, the apparent power dependence of the decay on n_s in the reversible regime, and a leveling off for the highest reversal amplitude, is consistent with the observation of a reversible-irreversible transition observed in [80]. However, as illustrated in Fig. 5.7c, f_b cannot identify this local reversibility in the neighbor network over the period of one cycle - f_b after one cycle increases approximately linearly with cycle amplitude without a clear change in the form of the dependence on $\Delta\theta$.

5.6 Fracture Dynamics

The analysis in this section was performed by Mitch Mailman.

Perhaps the most telling indicator of relative reversibility is the behavior of the Giant Component of the Broken Link Network. For all initial network cases, the scatter plot of Giant Component size s_g versus fraction of links broken f_b (Figure 5.9b) tend to fall along a curve (albeit with considerable noise) similar in magnitude to the curve shown for the steady shear case in Figure 4.7b. This suggests that the relationship between s_g and f_b is generic, at least for granular Broken Link Networks in the split bottom geometry.

The behavior of the Giant Component size further underscores the difference between small strain amplitude ($\theta_r \leq 20°$) and larger strain amplitude ($\theta_r \geq 40°$) cyclic strain. A stepwise plot of s_g versus strain for various strain amplitudes reveals that the Giant Component shrinks down considerably upon strain reversal for small strain amplitudes, but not for larger strain amplitudes (Figure 5.9a inset). This behavior persists for all choices of initial strain cycle, as seen in Figure fig5.899a. Apparently, after a critical strain between 20° and 40°, the nearest neighbor network is permanently broken.

5.7 Conclusions

Trajectory data from the RIMS apparatus on the split bottom shear cell reveals a partial reversibility in a granular flow subject to cyclic shear. CMSD data suggests that the grains move in a manner that has a reversible component and an irreversible component. Furthermore, as the system is subjected to more strain cycles, the irreversible component is reduced for small amplitudes. Network analysis suggests critical strain amplitude beyond which system-wide rearrangements may not be undone.

In future work, we would continue this experiment for strain amplitudes between 20° and 40° to test the nature of this cross-over from increasingly reversible cyclic shear flows to consistently irreversible cyclic shear flows. Furthermore, we would want to perform segregation experiments in this geometry to see whether small strain amplitudes are also reversible for bidisperse mixtures.

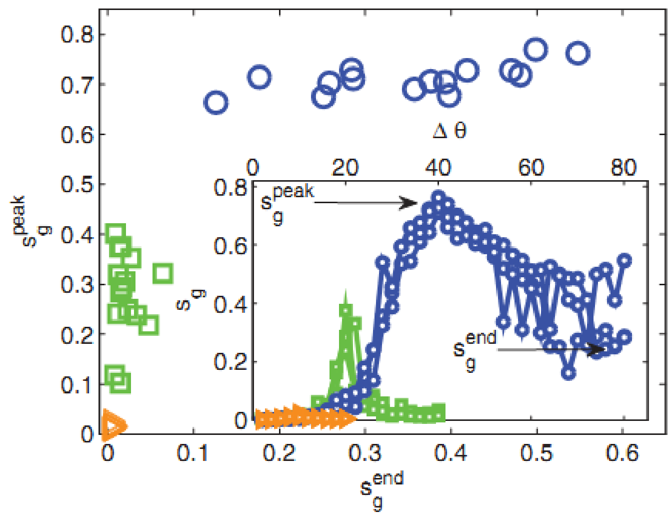

(a)

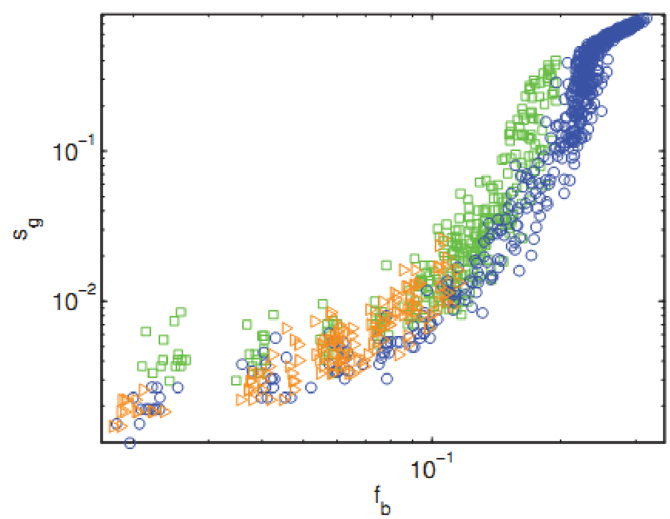

(b)

Figure 5.9: Behavior of the Giant Component (s_g of the Broken Link Network of a system Under Cyclic Shear (a) The peak of the Giant Component size versus the final Giant Component size, for each cycle. *Inset:* s_g as a function of the fraction of $\Delta\theta$ over one cycle for $n_s = 5$, 10, and 15. Peak and end values for s_g are highlighted for the 40° case. (b) s_g as a function of links broken f_b for each reference network used, for strain amplitudes of 10° [(orange) triangles], 20° [(green) squares], and 40° [(blue) circles].

Chapter 6

Future Uses of the RIMS technique

In this chapter, we discuss scenarios wherein the RIMS method can be employed to grains of different shapes and sizes. First, we demonstrate how we can image systems with non-spheroidal shapes. We then turn our attention to specially shaped particles, balls with holes drilled through the centers, for which we can find both centroids and orientation. Finally, we show that, with a slight modification to our image processing procedure, we can find and track spherical grains of different sizes.

6.1 Imaging Solids of Arbitrary Shape

The RIMS method is not dependent on the shape of the solid pieces in the interstitial fluid. As long as the solid is index-matched with the fluid, a cross-section of said solid within the path of a laser sheet will appear dark relative to the surrounding fluid. This works well with our Triton X-100/PMMA system, wherein we are able to see distinct cross-sections of PMMA blocks and rods. It stands to reason that we can image any solid shape, provided its main features are within the resolution of the imaging camera.

Although it is straightforward to image these shapes, it is much more complicated to find and track them automatically. We are not able to exploit the spherical

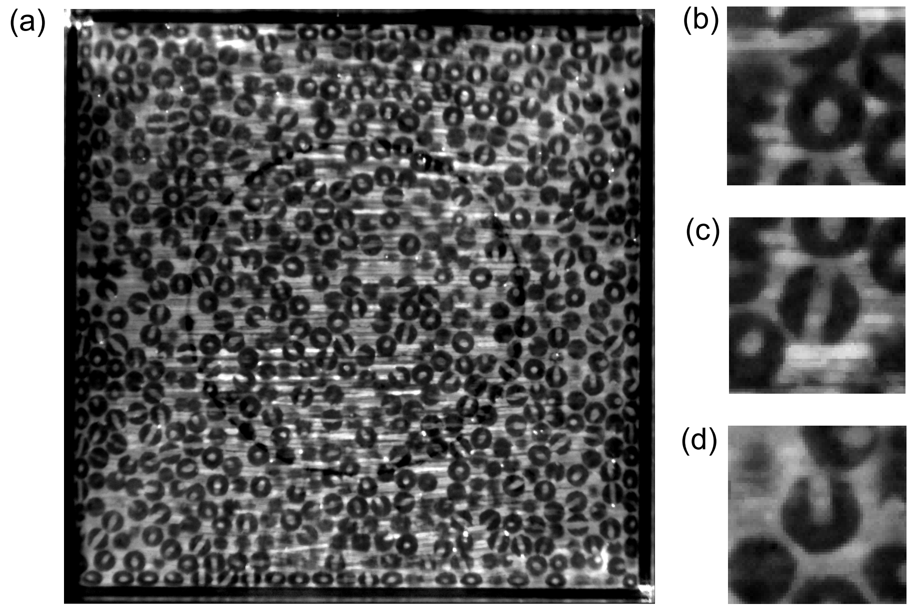

Figure 6.1: rotations

symmetry that our spherical grains possessed. However, it should be possible to adapt some more sophisticated methods, such as a Watershed Algorithm [81] to segment the 3D image and thus find the desired shapes.

6.2 Rotational Motion

Our grains can be modified to indicate their orientation in the RIMS system. The RIMS system allows us to image grains of any shape or size, as long as the material is index-matched. By simply substituting solid spherical grains with grains with cylindrical holes through their center, we can introduce grains that are easy to track, yet have orientational information as well.

The particle detection routine is a two stage process. First, we locate the grain centers using the usual routine. This is possible because the extraction routine is essentially an edge-finding algorithm which disregards most information within a spherical shell. After we have the centers, we can use the image intensity data immediately surrounding the centroids to calculate a covariance matrix. The orientation of the grain can then be determined by finding the dominant eigendirection of the covariance matrix.

Preliminary tests of this method have been quite promising. Grain orientations appear to faithfully indicate the orientations of the internal cylindrical holes. Furthermore, the angular resolution of the orientation is quite high (roughly 2° in a given plane, based on angle bias observed in initial trials). It should be possible to compare our results to those in previous studies of rotations in grains, such as the recent study by Nichol et al. [31].

6.3 Bidisperse Granular Flows

We can also use the RIMS method to track grains of multiple sizes. We can fill our shear cell system with equal masses of PMMA beads of two different sizes: 1/8" and 3/16". Since the grains are made of the same materials, we can use the same exact RIMS technique that we used for the case of the single grain size.

We only need to make a single modification to our image processing technique to find the grain centroids. We apply two different convolution kernels to the z-stacks, both of which are chosen to match the apparent diameter of both grain sizes. We find that, for our choice of grain sizes, the two convolved images are sufficiently distinct enough to find the centroids of small grains separately from large grains.

Thus, any bidisperse system where the large grains are 50% larger than the smaller grains is suitable for analysis using the RIMS method.

The following results have been generated by Matt Harrington with initial guidance from Steven Slotterback

Now that we are able to distinguish between large and small grains in a bidisperse system, we can measure the grain-level motions at the onset of a segregation process. Segregation occurs when an grains of different sizes in an ensemble migrate towards liked size grains under agitation. Common examples include segregation induced by vibrations [82] or shear forcing [83].

We can used our modified split-bottom system to track an entire shear-induced segregation process. We set our bidisperse system in our split-bottom shear cell and scan the system after 2° increments of strain from the shearing disk. We observe from z slices taken at the same height at different times (Figure 6.2) that the large and small grains separate after several revolutions of the shearing disk. Such data provide new avenues of analysis of shear induced segregation processes previously studied by others [84].

6.4 Summary

There are are several potential applications for the RIMS method to the study of granular flow. Although they may require additional image processing techniques, it is possible to use RIMS to explore dense granular flows of aspherical, polydisperse systems. In some cases, we can even measure rotations of individual grains. The

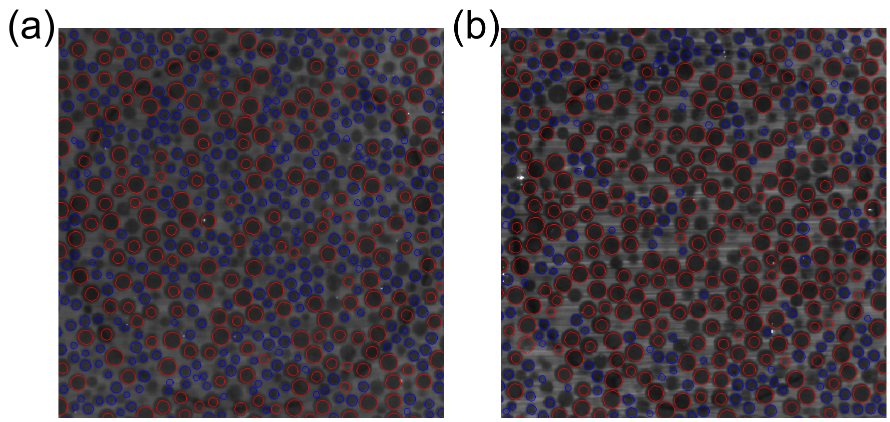

Figure 6.2: *Images in figure made by Matt Harrington* Sample trajectories of a bidisperse granular material undergoing segregation, as viewed using the RIMS split bottom system. Cross-sections of large (3/16 inch) grains are outlined in red, while small (1/8 inch) grains are outlined in blue. Both images are taken roughly 8 mm beneath the surface of a 46 mm pile of grains with an equal mass ratio. (a) The cross-section is taken at the beginning of the shearing process. (b) The cross-section is taken after the shearing disk has been rotated by 29.3 revolutions. The large and small grains have visibly segregated between the two frames.

versitility and relative affordability of the RIMS method compared to other 3D imaging schemes makes it a likely choice for future study of dense granular flows in general.

Chapter A

Motion Control System and Code Base

A.1 Motion Control

A.1.1 Overview of System

The RIMS apparatus is a custom system. It consists of:

- a specimen of grains with dyed index-matched fluid
- a CCD camera (PCO SensiCam 370 KL) with a PCI interface
- three separate stepper motor (Vexta PK266 -03B) driven linear actuators (Velmex Bi-Slide Assemblies), two for the laser line generators and one for the camera, controlled by a pair of digital controllers(Velmex VXM)
- a servo motor (Pacific Scientific PMA 24C) with a 25:1 ratio planetary gearhead (Thomson DynaTrue dt60-025) powered by a driver (Pacific Scientific PC833), controlled via a digital I/O DAQ board (Measurement Computing PMD 1208LS)
- a computer to control the camera, motor controller, and DAQ board

A schematic of the system is shown in Figure A.1.

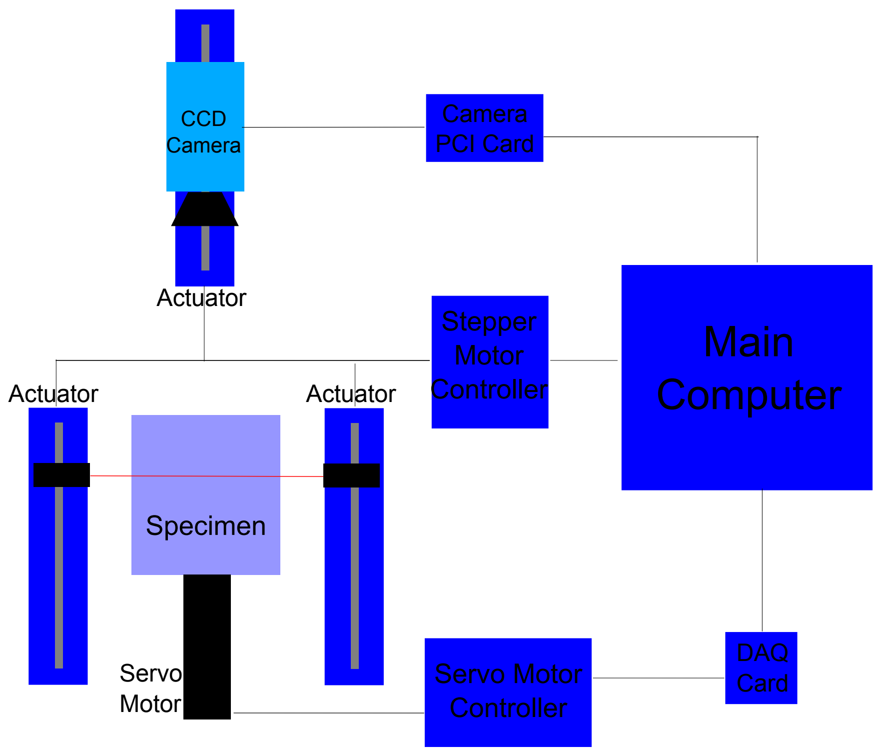

Figure A.1: System control schematic for RIMS apparatus

A.1.2 System Preparation

The first step in preparing the system is to make certain that the laser sheets are aligned properly. This step is performed manually. The sheets are aligned when both sheets are level at all distances (determined using levels) at the same height (determined using translucent paper as a guide). The actuators are then manually adjusted so that the sheets are just above the bottom surface of the containing vessel.

Once the laser sheet is in place, we configure the camera. We use the included software (SensiControl) to preview the image. We focus the camera lens until the features at the bottom of the vessel, particularly the outline of the shearing disk), are in focus. From this point on, the system is shielded from external light. We then use the software to maximize the exposure time of the camera so that the light from the laser sheet registers just below the maximum value allowed by the CCD chip, determined by taking a histogram of the preview image. We then crop the image so that only the laser sheet is visible, noting the apparent width of the box in order to set the pixel conversion scale.

Finally, we configure the servo motor driver for the shearing disk. For this step, we interface with the driver directly using the included software (Pacific Scientific 800 Tools). In brief, we configure two modes of motion: clockwise rotation of 50° (9102/65536 resolver counts) at a rate of 0.25 RPM, and counterclockwise rotation of $-50°$ (-9102/65536 resolver counts) at a rate of 0.25 RPM. We then disconnect the driver from the computer and configure the DAQ board and motor driver interface in order to choose between these two modes of control on command.

A.1.3 Motion Control Code

The system is controlled through a single set of C++ code. The code is commented internally to further explain where to make changes to perform different experiments.

- **CouetteBox[Experiment Name].cpp: Main Control Program**
  - ***Inputs*: filePath, laserSheetIncrement, cameraIncrement, numberImages, numberCycles,framesPerCycle**
  - ***Side Effects*: Takes images of z-slices of system, saves images to disk, controls shearing disk.**
  - ***Outputs*: N/A**
- **camera.h, camera.cpp: abstract camera control class code**
- **sensicamcamera.h, sensicamcamera.cpp, Senntcam.lib, Senntcam.dll: SensiCam Camera control code.**
- **CImg.h, tiff.h, tiffio.h, tiffvers.h, tiffconf.h, lifflib.lib: TIFF image generation code.**
- **VXMdriver.h, VXMdriver.cpp, VXMdriver.dll: VXM stepper motor contoller driver code.**

- **cbw32.lib, cbw32bc.lib, cbw.h: Digital I/O card (connected to servo motor) control code.**

A.2 In-House Particle Feature Extraction Routines (Matlab)

- **load_images.m: image loading and inverting script.**
  - ***Inputs*: Image path, xyz cropping parameters**
  - ***Function Calls*: None**
  - ***Side Effects*: None**
  - ***Outputs*: A 3 dimensional array containing all (intensity inverted) zslices in sequence.**
- **bpass_jhw.m: Performs a band pass on each z-slice**
  - ***Inputs*: z-slice, lnoise, lobject**
  - ***Function Calls*: None**
  - ***Side Effects*: None**
  - ***Outputs*: A spatially bandpassed z-slice.**
- **gauss_sphere.m: Creates convolution kernel.**
  - ***Inputs*: radius, sharpness_parameter, xyz kernel extent**
  - ***Function Calls*: None**
  - ***Side Effects*: None**

  - ***Outputs***: An appropriately sized convolution kernel for spherical edge finding.

- **analyze_scan.m: Feature extraction routine. Loads images, performs convolution operations, and finds grain centroids.**

  - ***Inputs***: Assumed grain diameter, edge finding sharpness parameter, z stack path, "Outpath" directory, xyz cropping parameters

  - ***Function Calls***: load_images.m, bpass_jhw.m, gauss_sphere.m

  - ***Side Effects***: None

  - ***Outputs***: An array of grain centroid data with five columns: x_c, y_c, z_c, i_max, i_total. i_max and i_total are the maiximum and total pixel values (respectively) with respect to each calculated centroid.

- **extra_scan_xxx.m: main feature extraction script. Assumes a "Main_Folder/Cycle/Frame" directory structure.**

  - ***Inputs***: Assumed grain diameter, edge finding sharpness parameter, "Main_Folder" path, "Outpath" directory, xyz cropping parameters

  - ***Function Calls***: analyze_scan.m

  - ***Side Effects***: Generates text files and MAT files with grain centroids for each z stack and places them into the "Outpath" directory.

  - ***Outputs***: None

- load_images.m: image loading script.

  - ***Inputs***: Assumed grain diameter, edge finding sharpness parameter, "Main_Folder" path, "Outpath" directory, xyz cropping parameters

  - ***Function Calls***: analyze_scan.m

  - ***Side Effects***: Generates text files and MAT files with grain centroids for each z stack and places them into the "Outpath" directory.

  - ***Outputs***: None

Appendix B

Particle Feature Extraction Methods

Once a three dimensional image of the granular pile is acquired, the centers of the grains are determined using digital image processing techniques. The grains appear as distinct, ball-shaped features in our three dimensional images. We employ a convolution scheme to our images to highlight the centroids of our grains to a high degree of precision. We use a displacement minimization algorithm to follow their trajectories through a series of 3D images.

In all cases, we assume that the length scale along the scanning dimension is equal to the length scale in each image plane. In practice, we must follow a protocol (see Appendix B) to both measure the pixel scale and adjust the z-slice scanning intervals.

B.1 Image Preprocessing

We employ methods to transform the grains in our images from dark balls into bright dots located at or near the centroids of those balls. As a first step, we always invert the image, so that the apparent brightness of the grains is higher than that of their surroundings. We typically use a filter of the form:

$$I'(x, y) = A - BI(x, y) \tag{B.1}$$

where A and B are typically positive constants chosen to maximize the contrast in the final processed image.

Over the course of this research, we have used two distinct methods to transform the grains into bright spots: the spatial band-pass filter method and a custom edge-finding method developed by Tsai and Gollub [85].

B.1.1 Band Pass Filtering

One method for processing the image is to apply a band-pass filter. For this method, the image is convolved so that features of a presumed size $2w + 1$ are enhanced, while features smaller than a size λ are smoothed out. The convolution kernel $K(x, y, z)$ is constructed in a method similar to that shown in [32]. The 3D generalization of their algorithm is:

$$K(i, j, k) = \frac{1}{K_0}\left[\frac{1}{D}\exp\left(-\frac{i^2 + j^2 + k^2}{4\lambda^2}\right) - \frac{1}{(2w + 1)^3}\right] \tag{B.2}$$

where $D = [\sum_{i=-w}^{w} \exp(-(i^2/4\lambda^2))]^3$ and $K_0 = 1/D[\sum_{i=-w}^{w} \exp(-(i^2/4\lambda^2))]^3 - (D/(2w + 1)^3)$. This method does not assume anything about the shape of the features in question save for the approximate size.

B.1.2 Tsai-Gollub Method

In the method put forth by Tsai and Gollub [85], we take advantage of the ball-like shape of the grain images, as well as their sharp intensity gradients along their boundaries. We convolve the inverted images with the following kernel, here

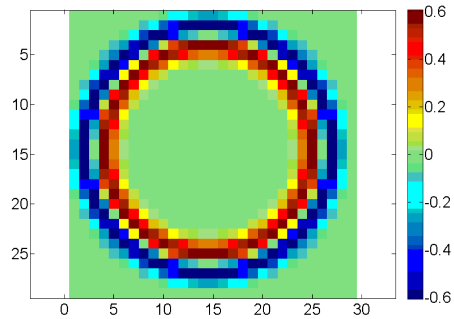

Figure B.1: Cross-Section of Sample Convolution Kernel at $z = a$, where $a = 15$. Spatial units are voxels and intensities are in arbitrary units.

written in spherical coordinates:

$$M(r) = -\frac{\sqrt{2}(r-a)}{\sigma} e^{\frac{-(r-a)^2}{2\sigma^2}} \tag{B.3}$$

where a is the presumed grain radius (in pixels) and σ is the inversely proportional to the steepness of the gradient along the boundary of the grain. The extent of the kernel is chosen to be cube of size $2.5a$ centered about a (see Fig. B.1). It is notable that the mean value of this kernel is negative, due to the negative region immediately outside of the spherical edge is larger than the positive region immediately inside of the spherical edge.

B.2 Peak-Finding Methods

Once the convolution has been applied to our image, we are in a position to extract our grain centroids, which appear as "bright spots," or relative maxima, in the resultant image. There are many methods for finding local maxima in images.

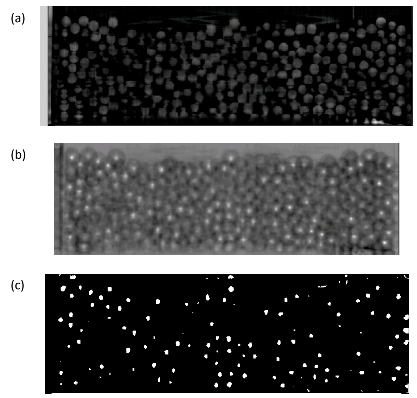

Figure B.2: Vertical Cross-section (reconstructed) of 3D image after (a) inversion and background filtering, (b) convolution with kernel as defined in equation B.3, (c) thresholding.

Here, we explore two schemes for finding distinct maxima. The first, developed by Crocker and Grier [32], is commonly used in the literature [86]. The second, developed in-house by Joost Weijs, is the method used to generate the results presented in this work.

Both methods use a thresholding criterion on the convolved image before labeling the centroids. The alternative method that we use to find the centroids is the thresholding method. In this method, we convert the image to binary using the following criterion:

$$I_{thresh}(x,y,z) = \begin{cases} 1 & I_{convol}(x,y,z) \geq I_t \\ 0 & r < I_t \end{cases} \tag{B.4}$$

where I_t is a threshold value chosen so that the peaks about the presumed grain centroids appear distinct yet are several voxels in extent. The two methods diverge from there.

B.2.1 Grier-Crocker Method

The common method, developed by Crocker and Grier, is essentially a peak finding algorithm. First, the thresholded image is used to mask insignificant voxels as follows:

$$I_{peakfind}(x, y, z) = I_{convol}(x, y, z) * I_{thresh}(x, y, z) \tag{B.5}$$

where $*$ is an element-wise multiplication. All voxels not on the borders of the image are then compared to their adjacent voxels (26 in 3D forming a cube about the initial voxel). If they are the highest in their immediate neighborhood, their position is included in a list of candidate peaks. Finally, if a given candidate is considered a "true" peak if it is a candidate peak that has no greater candidate peaks within a set distance R_p.

Once the relevant peaks are found, the intensities of the surrounding voxels are used to determine the centroids of the features in which the peaks were found. All the voxels with $1.5R_p$ of a given peak are used to used to create a collection of voxels P_i about the i-th peak. The centroids are found using the following formula:

$$\vec{X}_i = \frac{\sum\limits_{j \in P_i} I_{convol}(\vec{x}_j)\vec{x}_j}{\sum\limits_{j \in P_i} \vec{x}_j} \tag{B.6}$$

B.2.2 Thresholding Method

We present a refinement of the Crocker-Grier method for finding grain centroids. Rather than looking for local maxima for centroid candidates, we use entire contiguous regions to find the candidate grain regions P_i. The contiguous regions are found using a variation of the union-find algorithm such as described in [87].

The cetroids are then calculated as in equation B.6.

B.3 Quality Control Methods

The automatic centroid finding methods, while precise, are not infallable. For instance, it is possible for undesirable features in the images, such as scattered light from small air bubbles, to create local intensity distortions. Also, slight mismatches in the refractive index between grains and fluid can create bright streaks due to lensing. These distortions can affect our centroids in unpredictable ways. Therefore, we compensate for these problems by eliminating false positive centroids and, when necessary, manually inserting likely centroids manually.

B.3.1 Excluding False Centroids

We exploit the fact that false positive centroids, particularly in noisy regions of our images, tend to have weaker intensity signatures than average. Furthermore, they are sometimes also We see these low intensities in a log-log scatter plot of total centroid intensity vs. the maximum single intensity value of each found grain, as in Figure B.3. We can eliminate most of these false centroids by either choosing a minimum peak intensity (usually by shifting the threshold cutoff) or by choosing a cutoff for minimum total intensity to retain. Both methods eliminate most of the same bad centroids, albeit with relatively small differences. We use the latter criterion (total intensity minimum) in this work.

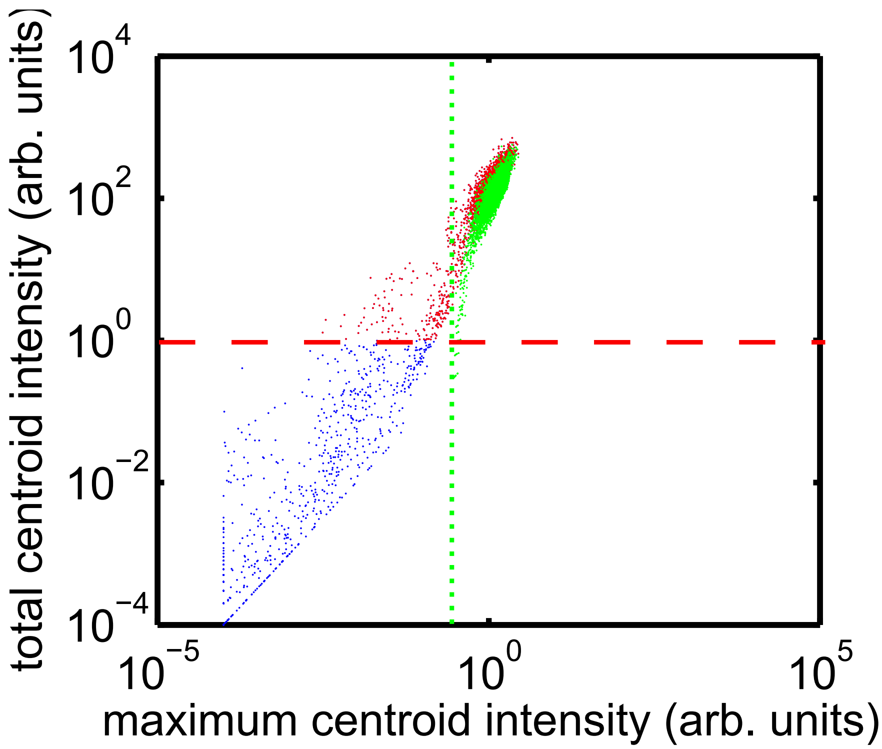

Figure B.3: Comparison of Two Methods of Exclusion of False Positive Centroids. A scatter plot of total centroid intensity vs. maximum centroid intensity for a sample frame from the split-bottom shear cell (blue and red plots). Thresholding (green).

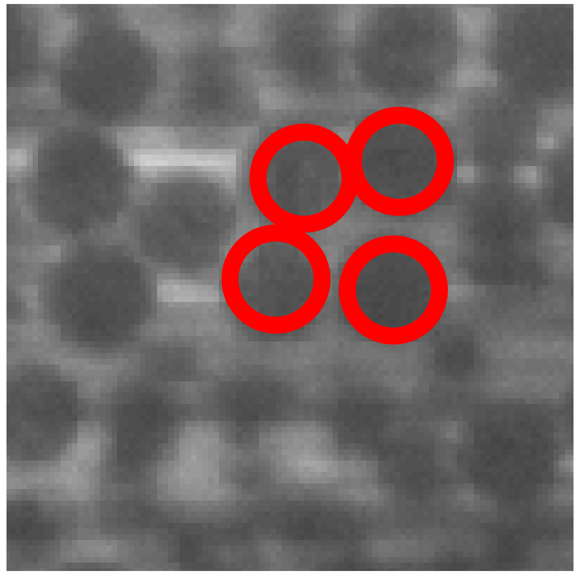

Figure B.4: Sample z slice with manually selected centroids shown outlined in red.

B.3.2 Incorporating Missing Centroids

After we eliminate false centroids, we turn our attention to locating regions where grain centroids may have been missed. We use the locations of the centroids to draw projected outlines of grain surfaces onto the original digital image stacks of the system. We inspect the images for features that appear to be grain cross-sections, yet have no outline. We find the z slice where the suspected grain has the largest cross-section, and manually select the pixel location closest to the center of said cross-section. This method is less precise, as it is limited by both the pixel scale of the image and the judgement of the user. Given the reduced precision of this manual location method, we use it only after all other means of improving image quality have been exhausted. (See Figure B.4)

B.4 Discussion

In summary, we have two primary methods at our disposal for locating centroids of grains in our 3D images. The Crocker-Grier code is ubiquitous in the literature, but does not take advantage of the characteristic features of the grain images. Our methods, on the other hand, exploit the steep gradients at the borders of the grains to get more precise centroids. Also, in the worst cases, we are able to eliminate false centroids and manually add missing centroids when necessary.

Bibliography

[1] K. Chen, J. Cole, C. Conger, J. Draskovic, M. Lohr, K. Klein, T. Scheidemantel, and P. Schiffer. Packing grains by thermal cycling. *Nature*, 442:257, 2006.

[2] T. Aste, T. Di Matteo, M. Saadatfar, T. J. Senden, Matthias Schrter, and Harry L. Swinney. An invariant distribution in static granular media. *Euro. Phys. Lett.*, 79:24003, 2007.

[3] Xiang Cheng, Jeremy B. Lechman, Antonio Fernandez-Barbero, Gary S. Grest, Heinrich M. Jaeger, Greg S. Karczmar, Matthias E. Möbius, and Sidney R. Nagel. Three-dimensional shear in granular flow. *Phys. Rev. Lett.*, 96:038001, Jan 2006.

[4] M.A. Riner, M.S. Robinson, J.M. Eckart, and S.J. Desch. Global survey of color variations on 433 eros: Implications for regolith processes and asteroid environments. *Icarus*, 198(1):67, 2008.

[5] J. C. Laul, J. J. Papike, and S. B. Simon. The lunar regolith - comparative studies of the apollo and luna sites. chemistry of soils from apollo 17, luna 16, 20, and 24. *Proceedings of the 12th Lunar and Planetary Science Conference*, pages 389–407, 1982.

[6] Z Fournier, D Geromichalos, S Herminghaus, M M Kohonen, F Mugele, M Scheel, M Schulz, B Schulz, Ch Schier, R Seemann, and A Skudelny. Mechanical properties of wet granular materials. *Journal of Physics: Condensed Matter*, 17(9):S477, 2005.

[7] C. A. Coulomb. *Essai sur une application des règles de maximis & minimis à quelques problèmes de statique, relatifs à l'architecture.* De l'Imprimerie Royale, Paris, 1776.

[8] R. A. Bagnold. *The physics of blown sand and desert dunes.* Methuen, London, 1941.

[9] W.A. Beverloo, H.A. Leniger, and J. van de Velde. The flow of granular solids through orifices. *Chemical Engineering Science*, 15(3-4):260, 1961.

[10] Leonardo E. Silbert, Deniz Ertaş, Gary S. Grest, Thomas C. Halsey, Dov Levine, and Steven J. Plimpton. Granular flow down an inclined plane: Bagnold scaling and rheology. *Phys. Rev. E*, 64:051302, Oct 2001.

[11] G Mandl, L N J De Jong, and A Maltha. Shear zones in granular materials. an experimental study of their structure and mechanical genesis. *Rock Mechanics and Rock Engineering*, 9:95, 1977.

[12] K. M. Hill and J. Kakalios. Reversible axial segregation of binary mixtures of granular materials. *Phys. Rev. E*, 49(5):R3610–R3613, May 1994.

[13] John R. Royer, Eric I. Corwin, Andrew Flior, Maria-Luisa Cordero, Mark L. Rivers, Peter J. Eng, and Heinrich Jaeger. Formation of granular jets observed by high-speed x-ray radiography. *Nature Physics*, 1:164–167, 2005.

[14] R. M. Nedderman and C. Laohakul. The thickness of the shear zone of flowing granular material. *Powder Technol.*, 25:91, 1980.

[15] R. M. Nedderman. *Statics and kinematics of granular materials*. Cambr. Univ. Press, Cambridge, 1992.

[16] P. G. de Gennes. *Superconductivty of Metals and Alloys*. Addison-Wesley, 1989.

[17] P. Bak, C. Tang, and K. Wiesenfeld. Self-organized criticality: An explanation of $1/f$ noise. *Phys. Rev. Lett.*, 59(4):381–384, 1987.

[18] H. M. Jaeger, Chu-heng Liu, and Sidney R. Nagel. Relaxation at the angle of repose. *Phys. Rev. Lett.*, 62:40–43, Jan 1989.

[19] G. William Baxter, R. P. Behringer, Timothy Fagert, and G. Allan Johnson. Pattern formation in flowing sand. *Phys. Rev. Lett.*, 62:2825–2828, Jun 1989.

[20] J. Rosendahl, M. Vekić, and J. Kelley. Persistent self-organization of sandpiles. *Phys. Rev. E*, 47:1401–1404, Feb 1993.

[21] Hernán A. Makse, David L. Johnson, and Lawrence M. Schwartz. Packing of compressible granular materials. *Phys. Rev. Lett.*, 84:4160–4163, May 2000.

[22] Herbert Goldstein. *Classical Mechanics*. Addison-Wesley Publishing Company, Reading, MA, 2nd edition, 1980.

[23] S.F Edwards. The equations of stress in a granular material. *Physica A: Statistical Mechanics and its Applications*, 249(14):226 – 231, 1998.

[24] J. D. Bernal and J. Mason. Packing of Spheres: Co-ordination of Randomly Packed Spheres. *Nature*, 188:910–911, December 1960.

[25] F. Radjai and F. Dubois. *Discrete-Element Modeling of Granular Materials*. John Wiley & Sons, 2011.

[26] A. W. Lees and S. F. Edwards. The computer study of transport processes under extreme conditions. *J. Phys. C*, 5(6):1921, 1972.

[27] C. K. K. Lun and A. A. Bent. Numerical simulation of inelastic frictional spheres in simple shear flow. *J. Fluid Mech.*, 258:335, 1994.

[28] W. Losert, D. G. W. Cooper, and J. P. Gollub. Propagating front in an excited granular layer. *Phys. Rev. E*, 59:5855, 1999.

[29] Masahiro Toiya, Justin Stambaugh, and Wolfgang Losert. Transient and oscillatory granular shear flow. *Phys. Rev. Lett.*, 93:088001, 2004.

[30] Christian R. Berardi, Kipton Barros, Jack F. Douglas, and Wolfgang Losert. Direct observation of stringlike collective motion in a two-dimensional driven granular fluid. *Phys. Rev. E*, 81:041301, Apr 2010.

[31] Kiri Nichol and Karen E. Daniels. Equipartition of rotational and translational energy in a dense granular gas. *Phys. Rev. Lett.*, 108:018001, Jan 2012.

[32] J. Crocker and D. Grier. Methods of digital video microscopy for colloidal studies. *J. Colloid Interface Sci.*, 179:298, 1996.

[33] T. S. Majmudar and R. P. Behringer. Contact force measurements and stress-induced anisotropy in granular materials. *Nature*, 435:1079–1082, 2005. doi: 10.1038/nature03805.

[34] B. Utter and R. P. Behringer. Transients in sheared granular matter. *The European Physical Journal E: Soft Matter and Biological Physics*, 14:373–380, 2004. 10.1140/epje/i2004-10022-4.

[35] J. Zhang, J. Ren, S. Farhadi, R. P. Behringer, T. S. Majmudar, and A. Tordesillas. A dense 2d granular material subject to cyclic pure shear. *AIP Conference Proceedings*, 1145(1):553–556, 2009.

[36] K. Sakaie, D. Fenistein, T. J. Carroll, M. van Hecke, and P. Umbanhowar. Mr imaging of Reynolds dilatancy in the bulk of smooth granular flows. *EPL (Europhysics Letters)*, 84(3):38001, 2008.

[37] Ping Wang, Chaoming Song, Christopher Briscoe, and Hernán A. Makse. Particle dynamics and effective temperature of jammed granular matter in a slowly sheared three-dimensional couette cell. *Phys. Rev. E*, 77:061309, Jun 2008.

[38] L. Wang, J. Frost, and J. Lai. Three-dimensional digital representation of granular material microstructure from x-ray tomography imaging. *Journal of Computing in Civil Engineering*, 18(1):28–35, 2004.

[39] S.A. McDonald, L.C.R. Schneider, A.C.F. Cocks, and P.J. Withers. Particle movement during the deep penetration of a granular material studied by x-ray microtomography. *Scripta Materialia*, 54(2):191 – 196, 2006.

[40] T. Aste, M. Saadatfar, A. Sakellariou, and T.J. Senden. Investigating the geometrical structure of disordered sphere packings. *Physica A: Statistical Mechanics and its Applications*, 339(12):16 – 23, 2004. Proceedings of the International Conference New Materials and Complexity.

[41] Wouter G. Ellenbroek, Ellák Somfai, Martin van Hecke, and Wim van Saarloos. Critical scaling in linear response of frictionless granular packings near jamming. *Phys. Rev. Lett.*, 97(25):258001, Dec 2006.

[42] Masahiro Toiya, Jacco Hettinga, and Wolfgang Losert. 3d imaging of particle motion during penetrometer testing. *Granular Matter*, 9(5):323–329, 2007.

[43] Joshua A. Dijksman, Frank Rietz, Kinga A. Loerincz, Martin van Hecke, and Wolfgang Losert. Invited article: Refractive index matched scanning of dense granular materials. *Review of Scientific Instruments*, 83(1):011301, 2012.

[44] Persistence of Vision Pty. Ltd. Persistence of Vision Raytracer (version 3.62), 2009. http://www.povray.org/download/.

[45] Paul J. Steinhardt, David R. Nelson, and Marco Ronchetti. Bond-orientational order in liquids and glasses. *Phys. Rev. B*, 28:784–805, Jul 1983.

[46] Steven Slotterback, Masahiro Toiya, Leonard Goff, Jack F. Douglas, and Wolfgang Losert. Correlation between particle motion and voronoi-cell-shape fluctuations during the compaction of granular matter. *Phys. Rev. Lett.*, 101(25):258001, Dec 2008.

[47] A. Rahman. Correlation in the motion of atoms in liquid argon. *Phys. Rev.*, 136(2A):A405–A411, 1964.

[48] Inc. Staff Hendrickson Publishers and L.L.N.I.V. Bible. *The Holy Bible New International Version*. Hendrickson Pub, 2004.

[49] J. B. Knight, C. G. Fandrich, C. N. Lau, H. M. Jaeger, and S. R. Nagel. Density relaxation in a vibrated granular material. *Phys. Rev. E*, 51(5):3957–3962, 1995.

[50] G. C. Barker and Anita Mehta. Transient phenomena, self-diffusion, and orientational effects in vibrated powders. *Phys. Rev. E*, 47:184–188, Jan 1993.

[51] G. C. Barker and A. Metha. Transient phenomena, self-diffusion, orientational effects in vibrated powders. *Phys. Rev. E*, 47(1):184, 1993.

[52] Xu N.a b Chen D.T.N.a Yunker P.a Alsayed A.M.a Aptowicz K.B.c Habdas P.a Liu A.J.a Nagel S.R.b Yodh A.G.a Zhang, Z.a. Thermal vestige of the zero-temperature jamming transition. *Nature*, 459(7244):230–233, 2009. cited By (since 1996) 51.

[53] J. De Boer, J.M.J. Van Leeuwen, and J. Groeneveld. Calculation of the pair correlation function: Ii. results for the 12-6 lennard-jones interaction. *Physica*, 30(12):2265 – 2289, 1964.

[54] C. Bradford Barber, David P. Dobkin, and Hannu Huhdanpaa. The quickhull algorithm for convex hulls. *ACM Trans. Math. Softw.*, 22(4):469–483, 1996.

[55] Francis W. Starr, Srikanth Sastry, Jack F. Douglas, and Sharon C. Glotzer. What do we learn from the local geometry of glass-forming liquids? *Phys. Rev. Lett.*, 89(12):125501, Aug 2002.

[56] T. Aste and T. Di Matteo. Emergence of gamma distributions in granular materials and packing models. *Phys. Rev. E*, 77:021309, Feb 2008.

[57] S. F. Edwards and R. B. S. Oakeshott. Theory of powders. *Physica A*, 157:1080, 1989.

[58] Richard I. Shrager. Nonlinear regression with linear constraints: An extension of the magnified diagonal method. *J. ACM*, 17:446–452, July 1970.

[59] Robert Zwanzig and Marvin Bishop. Tunnel model of liquid diffusion. *The Journal of Chemical Physics*, 60(1):295–296, 1974.

[60] Jack F. Douglas, Jacek Dudowicz, and Karl F. Freed. Does equilibrium polymerization describe the dynamic heterogeneity of glass-forming liquids? *The Journal of Chemical Physics*, 125(14):144907, 2006.

[61] Claudio Donati, Jack F. Douglas, Walter Kob, Steven J. Plimpton, Peter H. Poole, and Sharon C. Glotzer. Stringlike cooperative motion in a supercooled liquid. *Phys. Rev. Lett.*, 80(11):2338–2341, Mar 1998.

[62] Aaron S. Keys, Adam R. Abate, Sharon C. Glotzer, and Douglas J. Durian. Measurement of growing dynamical length scales and prediction of the jamming transition in a granular material. *Nature*, 3:260–264, 2007.

[63] D. Fenistein and M. van Hecke. Kinematics – wide shear zones in granular bulk flow. *Nature*, 425(6955):256, 2003.

[64] Denis Fenistein, Jan Willem van de Meent, and Martin van Hecke. Universal and wide shear zones in granular bulk flow. *Phys. Rev. Lett.*, 92(9):094301, Mar 2004.

[65] Alexander Ries, Dietrich E. Wolf, and Tamás Unger. Shear zones in granular media: Three-dimensional contact dynamics simulation. *Phys. Rev. E*, 76:051301, Nov 2007.

[66] Philippe Ribière, Patrick Richard, Renaud Delannay, Daniel Bideau, Masahiro Toiya, and Wolfgang Losert. Effect of rare events on out-of-equilibrium relaxation. *Phys. Rev. Lett.*, 95(26):268001, Dec 2005.

[67] T. Divoux and J.-C. Géminard. Friction and dilatancy in immersed granular matter. *Phys. Rev. Lett.*, 99:258301, Dec 2007.

[68] D. J. Durian. Foam mechanics at the bubble scale. *Phys. Rev. Lett.*, 75:4780–4783, Dec 1995.

[69] Matthieu Wyart, Leonardo E. Silbert, Sidney R. Nagel, and Thomas A. Witten. Effects of compression on the vibrational modes of marginally jammed solids. *Phys. Rev. E*, 72:051306, Nov 2005.

[70] Gijs Katgert, Andrzej Latka, Matthias E. Möbius, and Martin van Hecke. Flow in linearly sheared two-dimensional foams: From bubble to bulk scale. *Phys. Rev. E*, 79:066318, Jun 2009.

[71] M. Herrera, S. McCarthy, S. Slotterback, E. Cephas, W. Losert, and M. Girvan. Path to fracture in granular flows: Dynamics of contact networks. *Phys. Rev. E*, 83(6):061303, Jun 2011.

[72] Andreea Panaitescu and Arshad Kudrolli. Spatial distribution functions of random packed granular spheres obtained by direct particle imaging. *Phys. Rev. E*, 81(6):060301, Jun 2010.

[73] MD Rintoul and S Torquato. Computer simulations of dense hard-sphere systems. *Journal of Chemical Physics*, 105(20):9258–9265, NOV 22 1996.

[74] M. E. J. Newman and D. J. Watts. Scaling and percolation in the small-world network model. *Phys. Rev. E*, 60:7332–7342, Dec 1999.

[75] Duncan S. Callaway, John E. Hopcroft, Jon M. Kleinberg, M. E. J. Newman, and Steven H. Strogatz. Are randomly grown graphs really random? *Phys. Rev. E*, 64:041902, Sep 2001.

[76] Steven Slotterback, Mitch Mailman, Krisztian Ronaszegi, Martin van Hecke, Michelle Girvan, and Wolfgang Losert. Onset of irreversibility in cyclic shear of granular packings. *Phys. Rev. E*, 85:021309, Feb 2012.

[77] Joshua A. Dijksman, Elie Wandersman, Steven Slotterback, Christian R. Berardi, William Derek Updegraff, Martin van Hecke, and Wolfgang Losert. From frictional to viscous behavior: Three-dimensional imaging and rheology of gravitational suspensions. *Phys. Rev. E*, 82(6):060301, Dec 2010.

[78] Kiri Nichol. *Fluidization and Fluctuations in Granular Systems*. PhD thesis, Universiteit Leiden, Leiden, Nederlands, 2011.

[79] A. Einstein. ber die von der molekularkinetischen theorie der wrme geforderte bewegung von in ruhenden flssigkeiten suspendierten teilchen. *Annalen der Physik*, 322(8):549–560, 1905.

[80] L. Corté, P. M. Chaikin, J. P. Gollub, and D. J. Pine. Random organization in periodically driven systems. *Nature Physics*, 4:420–424, May 2008.

[81] Rafael C. Gonzalez and Richard E. Woods. *Digital Image Processing (3rd Edition)*. Prentice Hall, 3 edition, 2007.

[82] J. B. Knight, H. M. Jaeger, and S. R. Nagel. Vibration-induced size separation in granular media: The convection connection. *Phys. Rev. Lett.*, 70(24):3728, 1993.

[83] Lindsay B. H. May, Laura A. Golick, Katherine C. Phillips, Michael Shearer, and Karen E. Daniels. Shear-driven size segregation of granular materials: Modeling and experiment. *Phys. Rev. E*, 81(5):051301, May 2010.

[84] Yi Fan and K. M. Hill. Shear-driven segregation of dense granular mixtures in a split-bottom cell. *Phys. Rev. E*, 81:041303, Apr 2010.

[85] J.-C. Tsai and J. P. Gollub. Slowly sheared dense granular flows: Crystallization and nonunique final states. *Phys. Rev. E*, 70(3):031303, Sep 2004.

[86] T. H. Besseling, M. Hermes, A. Fortini, M. Dijkstra, A. Imhof, and A. van Blaaderen. Oscillatory shear-induced 3d crystalline order in colloidal hard-sphere fluids. *Soft Matter*, 8:2931–2939, 2012.

[87] Thomas H. Cormen, Clifford Stein, Ronald L. Rivest, and Charles E. Leiserson. *Introduction to Algorithms*. McGraw-Hill Higher Education, 2nd edition, 2001.